INFERRING ERUPTION DYNAMICS FROM SEISMOMETER-DERIVED GROUND TILT

MEASUREMENTS: A CASE STUDY OF TWO END-MEMBER VOLCANIC SYSTEMS

by

Michael Christoffersen

B.S. University of Texas at Austin, 2019

A Thesis Submitted in Partial Fulfillment of the Requirements

for the Degree of

Master of Science

in

Geophysics

University of Alaska Fairbanks

August 2024

APPROVED:

Ronni Grapenthin, Committee Chair

David Fee, Committee Member

Jessica Larsen, Committee Member

Bernard Coakley, Chair

Department of Geosciences

Karsten Hueffer, Dean

College of Natural Science and Mathematics

Richard Collins, Director

Graduate School

Abstract

Modern broadband seismometers are inertial sensors, and are sensitive to ground tilt as a consequence of this design. We use broadband seismometers positioned on Mt. Erebus on Ross Island, Antarctica, and Augustine Volcano in the Lower Cook Inlet, Alaska, to recover tilt measurements during individual volcanic explosions to investigate the magmatic system configuration of each volcano. At Mt. Erebus, thought to be an end-member open conduit volcanic system, we find no evidence of tilting associated with the Strombolian explosions produced by the volcano. Because tilt preceding Strombolian explosions has been observed at other volcanoes, we interpret the lack of tilt at Erebus as evidence that its conduit system lacks any viscous plugging or mechanical restrictions that are necessary to generate explosion-related tilt. At Augustine Volcano we are able to measure tilt changes associated with each of the thirteen events during the explosive phase of its 2006 eruption. We use the tilt changes to invert for a dual deformation source model of a depressurizing open conduit above a depressurizing prolate spheroid. This deflation source geometry is in agreement with an existing magmatic system model developed with petrologic, seismic, and GPS data, offering further support to the existing model.

Acknowledgements

On a personal note, I would like to thank the many people who have supported me as I worked on this degree. My parents, Alice and Steve, and my sister, Anna, have given me endless encouragement and provided many of the opportunities that have led me to where I am today. I would also like to thank my partner, Indujaa, for her patience throughout this whole process and her willingness to take on a move from the Sonoran Desert to interior Alaska. Many of the graduate students in the Geodesy Group and Glaciers Group have become great friends and make working at the Geophysical Institute a fun experience. I would also like to thank my advisor, Ronni, who has given me lots of freedom to roam while working on this project but has always been available to answer questions or talk through a confusing problem.

Table of Contents

List of Figures

List of Tables

viii

Chapter 1: Introduction

Ground tilt measurements are valuable because they provide a relatively autonomous (particularly in the modern era) method to measure ground deformation due to fast or small events that are difficult to measure with other geodetic techniques. Many modern tiltmeters have resolutions of 10 nrad or less (Agnew, 1986). This extreme sensitivity allows detection of small or distal volcanic processes through the tilt fields they create.

Measurements of ground tilt have been recorded at volcanoes since at least the early 20th century. Jaggar (1920) noted variations in the null point (i.e., tilting) of a Bosch-Omori horizontal pendulum seismometer – an early type of inertial ground motion sensor installed at the Hawaiian Volcano Observatory on the north rim of Kīlauea Volcano's summit crater – that correlated with fluctuations of the lava lake level in the crater. Jaggar & Finch (1929) further increased confidence in this correlation through observations of rapid tilt changes related to fluctuations in lava lake level. They also measured a multi-year tilt trend that correlated with an inflation-deflation cycle of Kīlauea Volcano.

Tilt measurements have since found wide use in volcano monitoring (Dzurisin, 2003), and many of the early advances in tilt measurement technology were made by volcano observatories (e.g., Eaton (1959); Westphal *et al.* (1983)). Some notable uses of tiltmeters in volcano monitoring include the forecasting of six effusive eruptions at Mt. St. Helens, USA in 1981 and 1982 (Dzurisin *et al.*, 1983), the prediction of explosive activity at Semeru Volcano, Indonesia (Kuswandarto *et al.*, 2008), and decades of use in monitoring the effusive activity of Kīlauea Volcano, USA (Klein, 1984).

However, not many active volcanoes are instrumented with tiltmeters. The Aleutian volcanic arc is an example of this. While 30 historically active volcanoes are instrumented with over 200 broadband seismometers, only three volcanoes in the arc are instrumented with tiltmeters at the time of this writing.

Modern broadband seismometers, however, are inertial ground motion sensors which respond to tilt as a consequence of their design (Ackerley, 2014) like the Bosch-Omori horizontal pendulum seismometer. In turn, broadband seismometers have been utilized to recover tilt measurements at several volcanoes, including Anatahan (Wiens *et al.*, 2005), Stromboli (Genco & Ripepe, 2010),

and Fuego (Lyons *et al.*, 2012). Thus, recovering tilt from broadband seismometers, a commonly ignored independent observable of these instruments, can dramatically increase the amount of tilt data available.

Here, we first present a method of recovering tilt measurements from broadband seismometers that we have implemented in an open source software package and demonstrate its functionality by reproducing previously published work. We then investigate whether pre- or co-eruptive tilt has been recorded by broadband seismometers at the open system Mt. Erebus volcano in Antarctica, and during the 2006 eruption of Augustine Volcano in Alaska (Fig. 1.1). We investigate a broadband seismometer time series spanning 2003 to 2013 at Mt. Erebus, which produces frequent Strombolian explosions and is thought to possess an open upper conduit system, where gas slugs grow and ascend without significant restriction (Aster, 2003). We then analyze data from the explosive portion of the 2006 eruption of Augustine Volcano. In contrast to the apparently open magmatic system at Mt. Erebus, the explosive activity during the 2006 eruption of Augustine Volcano was caused by repeated lava dome formation and plugging of the volcano's conduit (Coombs *et al.*, 2010). Our tilt measurements at Mt. Erebus show no evidence of eruption-related tilting, suggesting that viscous plugging (Capponi *et al.*, 2017) or another mechanism of pressurization necessary to produce the tilts observed during Strombolian explosions at other volcanoes (e.g., Genco & Ripepe (2010); Iguchi *et al.* (2008); Lyons *et al.* (2012)) is missing at Erebus, further supporting prior inferences of an unrestricted shallow conduit system (e.g., Aster (2003)). At Augustine Volcano we observe tilt changes associated with individual explosions and invert for a dual-deformation source model that agrees well with a conceptual model of the magmatic system developed from petrologic studies and geophysical data (Benage *et al.*, 2021; De Angelis *et al.*, 2013, 2020).
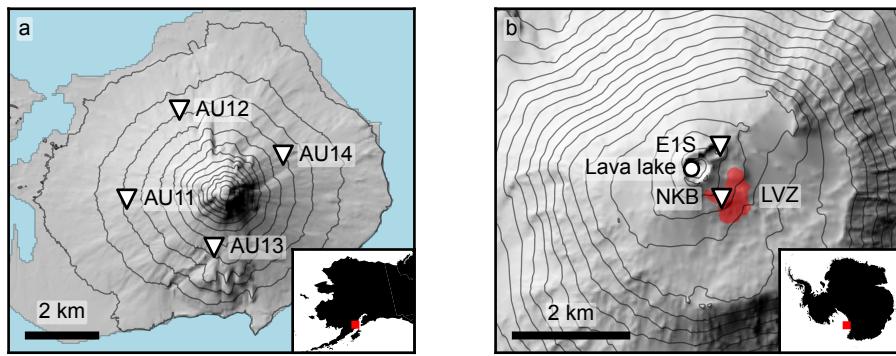
Figure 1.1: **a)** Hillshaded topographic map with 100 m contours of Augustine Volcano showing the locations of seismometers AU11, AU12, AU13, and AU14 used in this study. **b)** Hillshaded topographic map with 100 m topographic contours of Mt. Erebus showing the locations of seismometers NKB and E1S used in this study, the location of the persistent lava lake at the summit of Mt. Erebus, and the map location of the low velocity/high scattering zone inferred by Zandomeneghi *et al.* (2013) to be the location of a shallow magma reservoir (red area labeled "LVZ").

Chapter 2: Methods

2.1 Tilt Estimation From Broadband Seismometer Records

Ground tilt causes a signal in broadband seismometer data due to reorientation of the sensitive axes of the horizontal seismometer components with respect to gravitational acceleration. For a level, three-element seismometer with the elements oriented in a cardinal (east, north, up) configuration, the sensitive axes of the two horizontal elements are normal to the local gravity vector, so the signal output by each horizontal element does not contain any contribution from gravitational acceleration (Fig. 2.1a).

When the seismometer is rotated by ground tilt, the sensitive axes of the horizontal elements are no longer normal to the local gravity vector. Each horizontal element then experiences an acceleration (Eq. 2.1):

$$\ddot{x} = g \cdot \sin(\theta), \tag{2.1}$$

where $\ddot{x}$ is the component of gravitational acceleration experienced by the sensor, g is total gravitational acceleration, and θ is the angle between each element and its level position (Figure 2.1b). This relationship is nonlinear in θ. When θ is small, as is often the case for tilts caused by small or distal volcanic processes, it is appropriate to use a small angle approximation and simplify $\sin(\theta)$ to θ, making the acceleration experienced by each horizontal element (Eq. 2.2):

$$\ddot{x} = g\theta. \tag{2.2}$$

Similarly, when tilted by an angle θ, the vertical axis of the seismometer experiences an acceleration of $g \cdot \cos(\theta)$. This expression simplifies to g with a small angle approximation, meaning that the vertical axis of the seismometer is relatively insensitive to small tilts (Figure 2.1c).

It is impossible to conclusively disentangle acceleration due to translational motion from acceleration due to tilt in the output of a broadband seismometer. Wielandt & Forbriger (1999) pursued a model-based approach to separate the two signals, but the more common approach is to assume that all signals well below the natural frequency of the instrument are due to tilt. This is because sensitivity to tilt tends to dominate sensitivity to translational acceleration at long periods (Battaglia
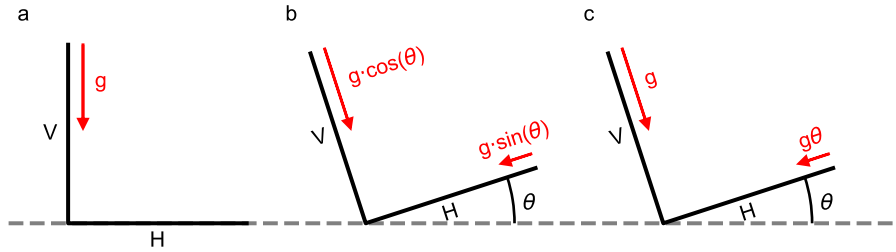
Figure 2.1: Three states of a hypothetical two element seismometer with a single horizontal element and a single vertical element. The red vectors and their labels represent the magnitude of gravitational acceleration sensed by the element, as a function of tilt angle θ in panels b and c. **a)** Gravitational acceleration experienced by each component when the instrument is level. **b)** Gravitational acceleration experienced by each component when the instrument is tilted by an angle θ. **c)** Small angle approximation of the gravitational acceleration experienced by each component when the instrument is tilted by an angle θ.

et al., 2000; Lyons *et al.*, 2012; Wiens *et al.*, 2005). As an example, Equation 2.2 gives that a 500 nrad amplitude tilt produces a signal equivalent to translational acceleration of $4.9\,\mu\text{m s}^{-2}$. At a 120 s period, doubly integrating the equivalent acceleration signal over one cycle yields a displacement of 2.2 centimeters. This shows that a much larger displacement than tilt is required to create equivalent equivalent signals in the seismometer record at long periods. Here we take the approach of assuming that tilt signals are dominant at periods much longer than the natural period of the instrument.

It follows from Equation 2.2 that the transfer function between tilt and and the voltage output of a broadband seismometer is a scaled version of the transfer function between translational acceleration and the voltage output of the instrument (Figure 2.2). To recover tilt from a broadband seismometer record we take the following steps:

1. Band-pass filter the recorded analog to digital converter (ADC) counts to the band of interest (generally tens of seconds to tens of thousands of seconds). The high frequency limit of the filter must be significantly lower than the corner frequency of the seismometer to satisfy the assumption of a tilt-dominated signal.

2. Calculate the transfer function between acceleration and recorded ADC counts of the seismometer-digitizer system using the `evalresp` program published by the Seismological Facility for the
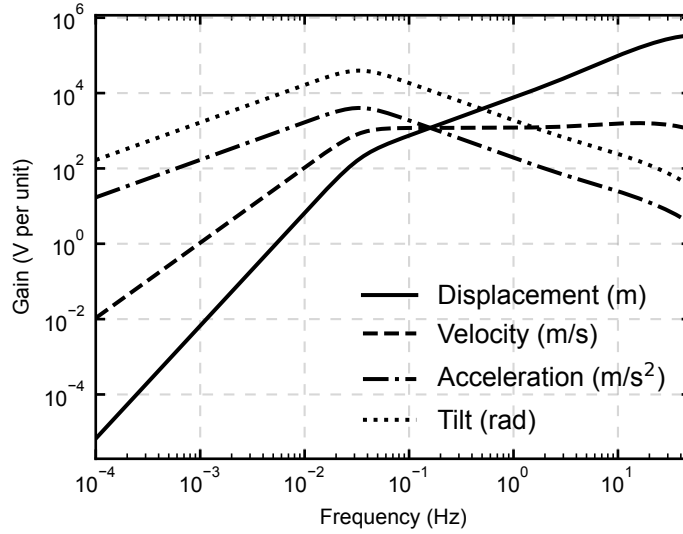
Figure 2.2: Transfer functions of a Guralp 6TD three component broadband seismometer, relating translational and small rotational motion to the voltage output of the instrument. As expected from Equation 2.2, the response of the instrument to tilt is a scaled version of its response to acceleration.

Advancement of Geoscience (SAGE) (Cooke & Dricker, 2022).

3. Multiply the acceleration transfer function by –g to obtain a tilt transfer function (Eq. 2.2).

4. Deconvolve the tilt transfer function from the band-pass filtered ADC counts time series by spectral division.

We implement this algorithm in an openly available software package written in the Python programming language (Christoffersen & Grapenthin, 2024). To validate our approach and implementation we reproduce published results at Anatahan Volcano (Fig. 2.3b includes the 24 hour tilt record shown in Fig. 3 of Wiens *et al.* (2005)).

Some modern seismometers do not have their sensing elements oriented in a true "cardinal" configuration with one vertical component and two horizontal, but instead have their elements arranged in a symmetric triaxial or "Galperin" configuration where the orthogonal sensing elements are rotated such that they are arranged symmetrically about the vertical axis (Ringler & Bastien, 2020). Data from seismometers with a symmetric triaxial configuration that has been rotated to cardinal components has the same sensitivity to tilt as a true cardinal seismometer, so seismometers utilizing both sensor configurations can be used for tilt studies (Graizer, 2009).

6

2.2 Horizontal to Vertical Power Ratio for Tilt Event Detection

In order to detect candidate ground tilt events, especially in years-long time series, we exploit the relative insensitivity of the vertical component of a broadband seismometer to small tilts (Fig. 2.1). Graizer (2006) demonstrates this vertical component insensitivity and uses a ratio of the smoothed Fourier amplitude spectrum estimates of horizontal and vertical component ground accelerations to estimate which frequency components of a broadband seismogram are tainted by a significant tilt signal during strong ground motion. In the presence of a significant tilt signal, the horizontal to vertical spectral amplitude ratio is elevated because tilting only contributes signal to the horizontal components. This phenomenon is demonstrated by Aderhold *et al.* (2015) as well, who note that an elevated horizontal to vertical spectral ratio at long periods is typical of broadband seismometer installations that are significantly affected by tilting due to environmental factors.

We develop a technique similar to the spectral ratio used in Graizer (2006) to detect segments of broadband seismometer data which may contain tilt signals. Instead of computing a spectral ratio, we estimate power in a band well below the corner frequency of the seismometer (e.g., zero frequency to 5 mHz) and compute the ratio of horizontal to vertical power. This approach helps to mitigate the noise that is inherently present in discrete Fourier transform-based power spectrum estimates (Wilson, 2021), because many samples of the noisy power spectral densities are used to compute the power estimates. For many sites, this power ratio will always be elevated (greater than one) due to tilting caused by environmental factors. Figure 2.3b presents an example of the power ratio based tilt detection. The horizontal to vertical power ratio in the east component of a seismometer at Anatahan Volcano in the Mariana Islands is greater than one preceding its 2003 eruption, presumably due to environmental tilting. Once the pre-eruptive volcanic tilt reported by Wiens *et al.* (2005) begins, the power ratio increases by nearly two orders of magnitude, a clearly detectable departure from the background ratio. We use Welch's method (Welch, 1967) to produce power spectral density estimates which we numerically integrate to compute power in the band of interest.

The power ratio approach is useful for detecting potential tilting because events that produce long period signals on all three components of a broadband seismometer, such as magnetic storms (Forbriger, 2007; Tape *et al.*, 2020) or very long period translational signals associated with volcanic phenomena (Aster, 2003), will not produce an elevated ratio. A drawback, however, is that tilting
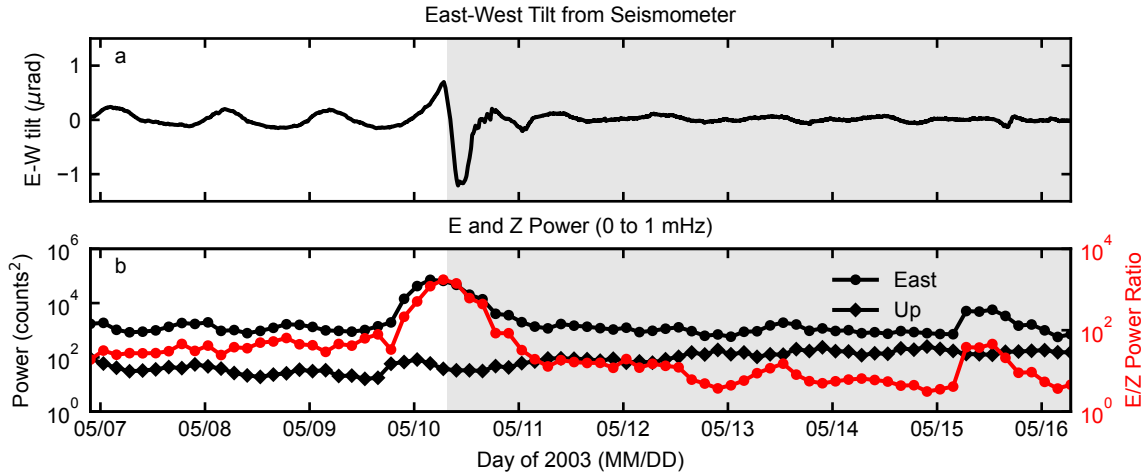
Figure 2.3: Elevated horizontal to vertical power ratio from tilting event at Anatahan Volcano immediately preceding its 2003 eruption (Wiens *et al.*, 2005). **a)** Seismometer-derived tilt from east channel. **b)** Power in east and vertical channels from 0 to 1 mHz for a moving 12-hour time window (black), and ratio of the two (red). Background shading in both panels shows time of active eruption.

during periods of elevated vertical component power may be obscured because the power ratio is suppressed. Figure 2.3 shows this: on May 15, there is a small potential tilt event leading to a relatively elevated power ratio (with respect to preceding ratio calculations), but high vertical component power prevents the power ratio from rising above the pre-eruptive level. The horizontal component power increases by nearly an order of magnitude without an accompanying increase in the vertical component power, which may allow identification of the potential tilt event through combined analysis of the horizontal component power and a horizontal to vertical power ratio.

2.3 Deformation Source Modeling

We use the Versatile Modeling of Deformation (VMOD) (Angarita *et al.*, 2024) software package to model deformation sources at Augustine Volcano, where we are able to measure co-eruptive changes in tilt. VMOD is an object-oriented framework that implements several analytical models for ground deformation caused by different types of buried pressure sources and dislocations (e.g., opening of a dike or slip on a fault). The analytical models that we utilize from VMOD are derived for the case of a homogeneous elastic half space. Topography and heterogeneous elastic properties in the subsurface can have a significant effect on displacement (e.g., Crozier *et al.* (2023)) and tilt

measurements (Harrison, 1976; Marsden *et al.*, 2019). We choose, however, to use the analytical models implemented in VMOD for this study because of their computational efficiency. Using the analytical models, we are able to perform probabilistic inversions requiring tens of millions of model runs, a process that would be computationally infeasible with a finite element model which could approximate the effect of topography and heterogeneous elastic properties on the tilt measurements. Additionally, the seismometers used for this study are positioned 1.5 km or more from the summit of Augustine Volcano on relatively low slopes of 5 to 12 degrees (Fig. 1.1a), which reduces the effect of topography (e.g., Crozier *et al.* (2023)), although the effects of deformation sources at higher elevation than the instrument can be complex (e.g., Lyons *et al.* (2012)).

Even in a homogeneous half space model, the tilt fields created by geometrically simple pressure sources, such as a prolate spheroid (Yang *et al.*, 1988), can be complex and difficult to interpret especially if sparsely sampled as is generally the case for volcano monitoring networks. Figure 2.4 shows a modeled vertical displacement field and the corresponding tilt field from a buried prolate spheroid experiencing depressurization. The vertical deformation field shows a decrease in magnitude near the center of the modeled domain but is uniformly negative, indicative of the depressurizing deformation source in the subsurface. The corresponding tilt field has an inner annulus of radial-outward tilt surrounded by an outer annulus of radial-inward tilt, as the tilt field is the gradient of the vertical deformation field. This complexity of tilt fields can make sparse measurements difficult to interpret without use of forward models – tilt measurements taken at various distances from the center of the domain shown in Figure 2.4 would show radial-outward tilt, no tilt, or radial-inward tilt, all resulting from the same depressurizing deformation source.
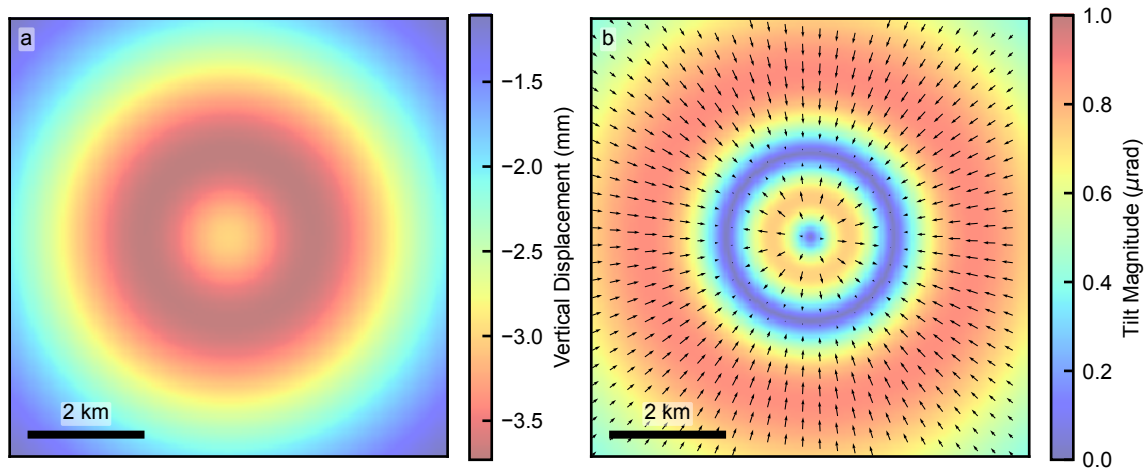
Figure 2.4: **a)** Vertical displacement from a depressurizing prolate spheroid source with a vertically oriented long axis centered in the domain shown. **b)** The tilt field created by the same deformation source, showing an annulus of radial-outward tilt that transitions to radial-inward tilt in the far field. The vectors show tilt direction and relative magnitude and the absolute tilt magnitude is shown as the colored background. The deformation and tilt fiends are calculated using the prolate spheroid deformation model of Yang *et al.* (1988). The prolate spheroid is experiencing a pressure change of –17 MPa and is located at the center of the domain at 3 km depth with a 1 km semi-major axis oriented vertically and a 250 m semi-minor axis

Chapter 3: Mount Erebus

3.1   Volcanic Context

Mt. Erebus is a stratovolcano on Ross Island, Antarctica that produces frequent Strombolian explosions and sustains a persistent phonolitic lava lake in its summit crater, at least since its discovery in 1973 (Giggenbach *et al.*, 1973). Seismological studies and the presence of a convecting lava lake suggest that the upper portion of Mt. Erebus' plumbing, where gas slugs form and ascend to the surface to create Strombolian explosions, is an open system (Aster, 2003; Gerst *et al.*, 2013; Knox *et al.*, 2018). Blick *et al.* (1989) measured approximately 50 mm of expansion across the crater of Mt. Erebus between 1980 and 1985 using a triangulation network. They also observed tilts in excess of $10\,\mu$rad during 1985 with a tilt leveling network, but attribute the tilts to ground instability at the monuments as opposed to volcanic activity due to their seemingly random orientations. More recently, GNSS observations show evidence of multi-year inflation-deflation cycles that are attributed to pulses of pressurization and depressurization, respectively accompanied by episodes of reduced and elevated explosive activity, or geometric changes in the shallow magmatic system of the volcano (Grapenthin *et al.*, 2022). We are not aware of any studies that investigate deformation associated with individual explosions at Mt. Erebus, a phenomenon which has been observed at other volcanoes producing Strombolian explosions (Genco & Ripepe, 2010; Iguchi *et al.*, 2008; Lyons *et al.*, 2012).

3.2   Data

At Mt. Erebus, we utilize data from permanent broadband seismometer installations maintained by the Mt. Erebus Volcano Observatory on the summit plateau of the volcano (Rowe *et al.*, 2000). We examine data from the two closest stations to Mt. Erebus' lava lake, E1S and NKB, for tilt associated with Strombolian explosions between 2003 and 2013. Figure 1.1b shows the location of the two instruments on Mt. Erebus' summit plateau. Both instruments are Guralp CMG-40T broadband seismometers with a 30 s corner period sampled at 40 Hz. There are significant gaps in data coverage due to power and telemetry limitations caused by the harsh environment of Mt. Erebus. However, there is generally good data availability during austral summers.
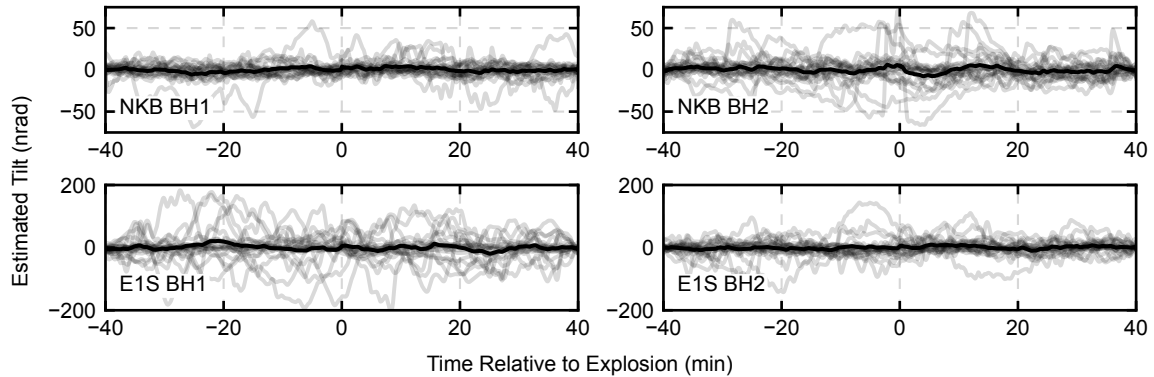
Figure 3.1: Tilt time series from the horizontal channels of seismometers NKB and E1S near the lava lake of Mt. Erebus for the ten largest explosions recorded from 2003-2013 in the catalog created by (Knox *et al.*, 2018) where data is available. Gray lines are tilt records from single explosions, each centered in time on the explosion. The solid black line in each panel is the station channel's mean tilt record calculated for the 10 explosions. The single event tilt records do not show any consistent change in tilt at time of eruption. The times of the events used in for this figure are given in Table A.1.

3.3 Tilt Records During Large Explosions

To search for tilt signals associated with Strombolian explosions at Mt. Erebus, we utilize an approach similar to that developed by Lyons *et al.* (2012) at Fuego Volcano and recover tilt in two hour windows centered on Strombolian explosions. We follow the deconvolution-based procedure detailed in the methods section of this paper to estimate tilt, filtering the raw seismograms to periods between 60 and 3600 s. We then calculate a mean tilt time series from the individual records, with the goal of coherently adding any eruption-associated tilt signals that may be too low in amplitude to confidently interpret from a single tilt record.

In Figure 3.1, we show the tilt records associated with the twenty largest explosions in the eruption catalog created by Knox *et al.* (2018) from seismic and infrasound data that have complete data availability for a two hour window at E1S and NKB. Most events used for Figure 3.1 occur during a period of increased eruptive activity in early 2007 (Fig. 3.2a). We see apparently random variation in the individual event tilt records that average to near-zero tilt at most time steps, suggesting that these tilt records show no consistent evidence of pre-eruptive or co-eruptive tilting.

12

3.4   Horizontal to Vertical Power Ratio From 2003 to 2013

Having found no evidence of systematic tilt associated with large Strombolian explosions at Mt. Erebus, we estimate a horizontal to vertical power ratio using all available data at NKB and E1S from 2003 to 2013 to comprehensively search for time periods of significant tilting or individual large tilt events. We estimate power spectral densities with Welch's method (Welch, 1967) from continuous twelve hour segments of data split into four hour sub-segments with 50% overlap. The resulting power spectral densities are integrated from zero to 1 mHz to estimate power.

Panels b and c in Figure 3.2 show the calculated horizontal to vertical power ratios at NKB and E1S. The power ratio time series at both stations show periods of increased horizontal to vertical power ratio, which may be indicative of tilting. However, when examining the raw seismometer outputs from these time periods it is apparent in all outputs that the elevated power ratio is due to instrumental or environmental noise. Panels d, e, and f in Figure 3.2 show examples of this: often only one horizontal element is affected by a signal with amplitude orders of magnitude higher than what is present on the other horizontal element, which is not plausible for a true tilt signal. We exclude all time periods where there is a factor of 100 or greater power difference between the two horizontal components from Figure 3.2. At some times, there is an elevated ratio present in both channels of a single seismometer (e.g., E1S in early 2009, see Figure 3.1c) but no apparent tilt signal is present on the other seismometer, which prevents confident interpretation. We chose not to rotate the horizontal seismometer components to radial/transverse with respect to the lava lake because the shallow magma reservoir inferred by Zandomeneghi *et al.* (2013) from the results of seismic tomography is a potential source of deformation as well. Additionally, the rotation would spread signal from a single malfunctioning horizontal component across both, and generate a signal that may appear more like a true ground tilt signal.

3.5   Discussion

These results indicate that Mt. Erebus does not experience short term inflation-deflation cycles associated with individual explosions in the manner observed at volcanoes such as Semeru (Iguchi *et al.*, 2008), Stromboli (Genco & Ripepe, 2010), and Fuego (Lyons *et al.*, 2012). The absence of this behavior at Mt. Erebus may be because it is an end-member among open conduit volcanoes. The convecting lava lake keeps the upper portion of the conduit hot, preventing the formation of a
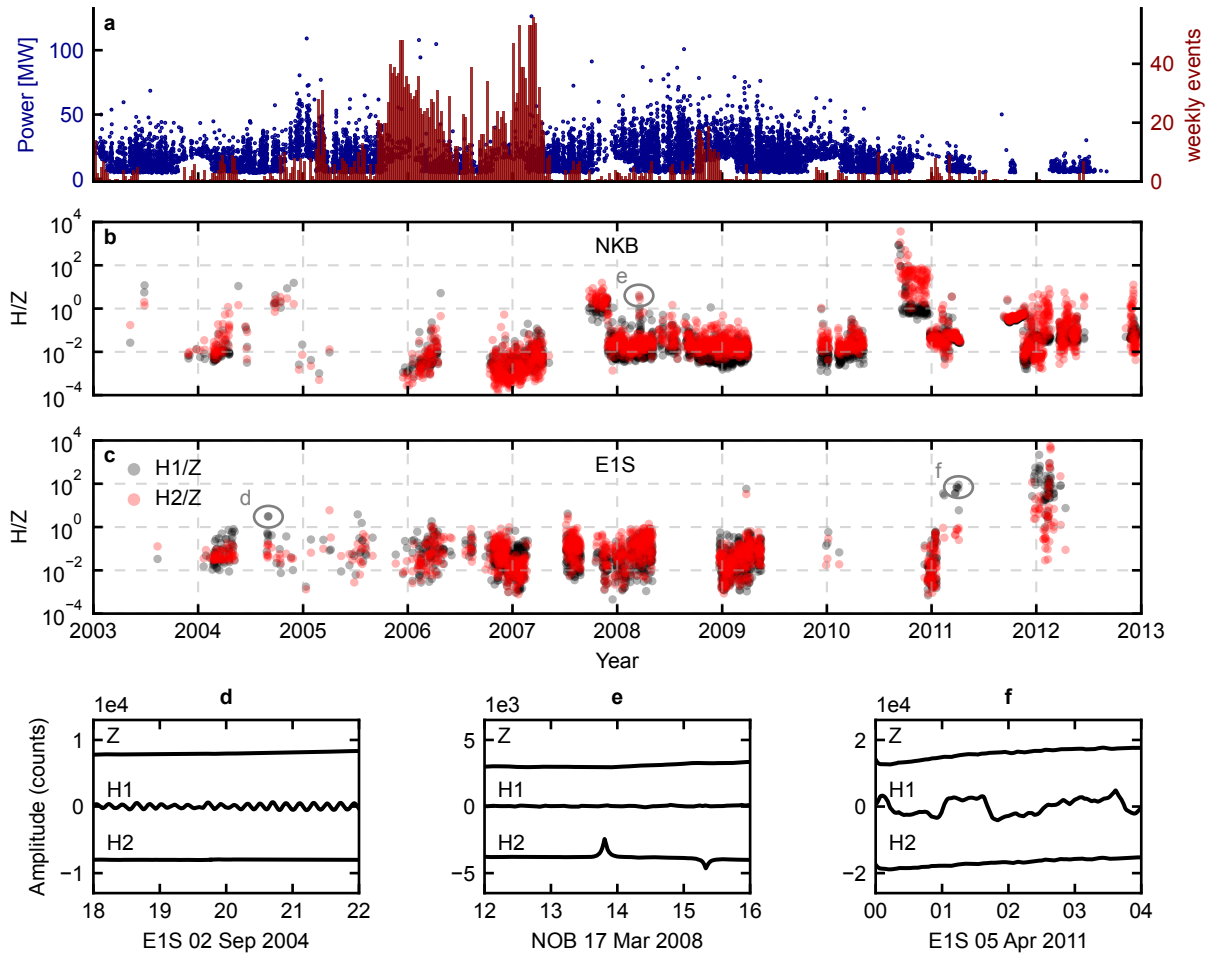
Figure 3.2: Horizontal to vertical power ratio in the 0 to 1 mHz band calculated for two seismometers on the summit plateau of Mt. Erebus. **a)** Scatter plot (blue) showing radiative power at the summit of Mt. Erebus derived from Moderate Resolution Imaging Spectrometer (MODIS) instrument using the MODVOLC program (Wright, 2016) and histogram (red) showing weekly eruption count estimated from seismic and infrasonic data, from Knox *et al.* (2018). Modified from (Grapenthin *et al.*, 2022). **b)** Horizontal to vertical power ratio over time at seismometer NKB. Red and black dots are the two horizontal components, which are not oriented to North and East for the entire data record. **c)** Horizontal to vertical power ratio over time at seismometer E1S, with the same symbology as panel b. We remove all time periods with a greater than 100x difference in power between the two horizontal seismometer channels, as that large of a power difference indicates malfunction of one of the sensors. Panels d, e, and f are characteristic examples of seismometer records leading to elevated horizontal to vertical power ratio in E1S and NKB. Grey ellipses and labels in panels b and c show the corresponding time periods. Locations of seismometers NKB and E1S are shown in Figure 1.1b.

14

viscous magma plug that has been shown to be important for eruptive dynamics at other volcanoes producing Strombolian explosions (Capponi *et al.*, 2017; McKee *et al.*, 2022).

A hot, mechanically unrestricted upper conduit may also allow pressure change preceding explosions to be accommodated by changes in the level of the lava lake instead of coupling into the edifice and causing deformation. Terrestrial laser scanning observations of the lake level appear to corroborate this, and have shown an increase in the level of the lava lake of 1.1 m preceeding an explosion followed by a decrease of multiple meters after (Jones *et al.*, 2015). Meter-scale changes in the level of the lava lake correspond to volume changes of thousands of cubic meters, similar to the slug volumes determined by Gerst *et al.* (2013) at Mt. Erebus.

The sparse measurement network we utilize at Mt. Erebus is another potential reason for the lack of observed tilt. Seismometers E1S and NKB are approximately 600 and 750 m away from the lava lake, respectively. Genco & Ripepe (2010) observe tilt on the order of tens of nanoradians on a tiltmeter at a similar distance from the vents at Stromboli, however. If the same tilt generation process was occurring at Mt. Erebus we would expect to see tilting of a similar magnitude, or perhaps even larger given that Mt. Erebus generates gas slugs with volumes of thousands of cubic meters (Gerst *et al.*, 2013) compared to slug volumes of tens of cubic meters at Stromboli (Ripepe & Marchetti, 2002) at similar overpressures. Noise in the broadband seismometer derived tilt records at Mt. Erebus may prevent detection of tens of nanoradian tilt changes in single event tilt records. The tilt records at NKB show tens of nanoradian scale noise, and at E1S the noise amplitude can exceed one hundred nanoradians (Fig. 3.1). However the stacking approach reduces the noise level at both stations to a level where a tens of nanoradian tilt change at explosion times would be apparent in the stacked time series.

Erebus is able to produce large gas slugs because of the large diameter of its upper conduit - the surface of the lava lake is 20 to 40 m in diameter and the lava lake is fed by a vent that is 5-10 m in diameter (Dibble *et al.*, 2008). A large conduit diameter can have a dampening effect on slug-caused deformation as well. In a large conduit, a gas slug can exist detached from the conduit wall, surrounded by a thick layer of magma instead of a falling film, reducing the ability of the high pressure inside of the slug to couple with the volcanic edifice and cause deformation (James *et al.*, 2006).

Very long period (VLP) (8-20 s) signals are consistently observed on broadband seismometers

at Mt. Erebus during Strombolian explosions (Aster, 2003). These VLP signals may contain a contribution from tilt in addition to translational motion, but are in a band above the corner frequency of the seismometer where translation and tilt both contribute significantly to the output of the instrument. Therefore we are not able to disentangle the two. These VLP signals are out-of-band for our analysis, which considers periods longer than 60 s (twice the corner frequency of the seismometers utilized). These signals may be the only deformational expression of the formation and ascent of gas slugs at Mt. Erebus, which is thought to occur in upper tens of meters of the conduit below the lava lake surface (Aster, 2003). Meter-scale gas slugs will have ascent rates on the order of meters per second at Mt. Erebus (De Lauro *et al.*, 2009), so ascent of a large bubble from shallow depths (Tens of meters) may only generate a deformation signal for tens of seconds.

Chapter 4: The 2006 Eruption of Augustine Volcano

4.1 Volcanic Context

Augustine Volcano is a stratovolcano in the Lower Cook Inlet of Alaska that has been active since at least the late Pleistocene and has had historic eruptions in 1883, 1935, 1964, 1976, 1986, and 2006 (Power *et al.*, 2010). The 2006 eruption of Augustine Volcano was particularly well monitored for an Alaskan volcano – successful detection of precursory activity by the Alaska Volcano Observatory allowed for the deployment of a network of seismic and GPS instruments on the volcano before the beginning of the eruption. The eruption can be divided into three phases: explosive, continuous, and effusive, each marked by changes in the character of the eruption (Coombs *et al.*, 2010). The explosive phase began on January 11 and lasted until January 28. During the explosive phase, there were 13 discrete explosions that produced approximately 30×10^6 m^3 dense rock equivalent (DRE) of material. The explosive phase was followed by a "continuous phase", where low level explosive activity produced nearly continuous block and ash flows from January 28 to January 31 then gradually waned until February 10. The continuous phase produced approximately 11×10^6 m^3 DRE of material. There was a pause in eruptive activity after the continuous phase until the beginning of the final effusive phase of the eruption in early March. The effusive phase of the eruption lasted until March 16 and produced approximately 26×10^6 m^3 DRE of material, mostly in the form of lava flows with occasional block and ash flows (Coombs *et al.*, 2010).

We focus our analysis on the explosive phase of the eruption, utilizing broadband seismometers to measure tilt changes associated with each explosion. All phases of the eruption were monitored geodetically with GPS (Cervelli *et al.*, 2010; Mattia *et al.*, 2008) allowing identification of deformation trends on time periods of days to years. Cervelli *et al.* (2010) observe extension between two GPS stations located on opposite sides of the volcano during the explosive phase, continuing a trend that began in September 2005, and greater than ten centimeters of displacement of a GPS station near the summit of the volcano on January 11, but these are the only explosive phase deformation observations reported. A high rate GPS analysis by Mattia *et al.* (2008) groups all phases of the eruption and approximately eight months of post-eruptive deformation into a single deformation phase.

4.2 Data

The Alaska Volcano Observatory (AVO) deployed five Guralp CMG-6TD broadband seismome-ters with 30 s corner periods sampled at 100 Hz on the flanks of Augustine Volcano to monitor its 2006 eruption (Alaska Volcano Observatory/USGS, 1988). Figure 1.1a shows the locations of each seismometer on the edifice. Data availability from the seismometers is good, with only short gaps (hours at most) during the explosive phase of the eruption. We utilize data from four seismometers: AU11, AU12, AU13, and AU14. The fifth (AU15) was deployed further from the summit of the volcano and not active during the explosive phase of the eruption.

4.3 Tilt Records During Explosions

To search for tilting during the 2006 eruption of Augustine volcano we estimate tilt time series during the explosive phase of the eruption, covering all thirteen documented explosions (Coombs *et al.*, 2010). Figure 4.1 shows tilt time series from seismometer AU12 during events 1 through 8. In the minutes after each explosion there is a significant change in tilt, often a microradian or more.

Figure 4.2 shows the tilt changes associated with each explosion. These tilt changes are mea-sured as the difference between tilt at each explosion and the tilt up to ten minutes after each explo-sion. The later measurement time is manually chosen per-event at the point of maximum monotonic tilt change. There are significant changes in the tilt signals from event to event. Figure 4.1b shows an example of this, where the tilt change in component HHE changes polarity between events 2 and 3 in the sub-panel. Some events show significant tilt anomalies, particularly event 12 where seismometer AU13 records tilt change greater than 150 μrad.

4.4 Deformation Source Modeling

We interpret the tilt changes following each explosion as a mixture of a regional deflationary signal, caused by depressurization of the volcano's conduit and subsequent mobilization of magma in the reservoir supplying the conduit, with tilt caused by deformation sources local to each of the seismometers. It is difficult to disentangle local and regional effects with a sparse measure-ment network. One potential source of local deformation is loading from mass flows caused by the explosions (Grapenthin *et al.*, 2010; Odbert *et al.*, 2015). Coombs *et al.* (2010) document many avalanche, pyroclastic flow, and lahar deposits that formed during the explosive phase of Augus-
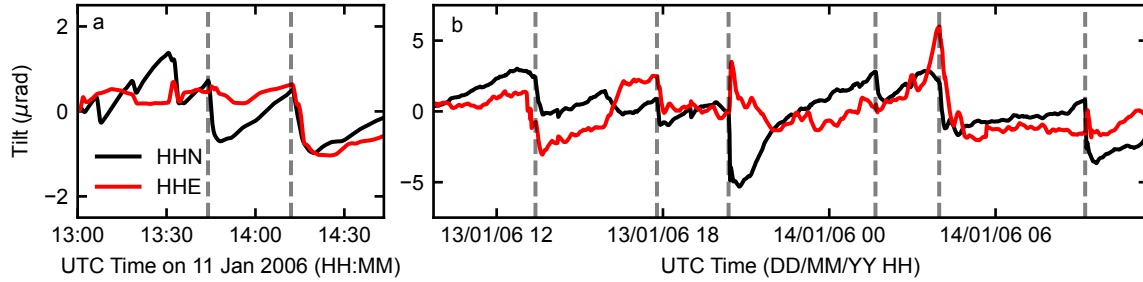
Figure 4.1: Tilt time series for the horizontal channels of seismometer AU12 during explosions **a)** 1-2 and **b)** 3-8 during the 2006 eruption of Augustine Volcano. Black lines are north-south tilt, where a positive value indicates tilting down to the north and red lines indicate east-west tilt, where a positive value indicates tilting down towards the east. The tilt time series are complicated and show some step changes that are not associated with recorded explosions, but at each recorded explosion there is a step change in tilt.

tine Volcano's eruption, some of which were deposited near broadband seismometer installations. Mass flows can cause significant tilt signals on broadband seismometers (Wenner *et al.*, 2022) and may explain some of the large event-to-event tilt differences. Figure A.2 shows per-event records of mass flows mapped by Coombs *et al.* (2010) compared to the tilt changes measured during each explosion. Many, but not all, of the significant event-to-event differences in tilt are associated with mass flows being emplaced near a seismometer. Additionally, the seismometer that is furthest from any recorded mass flows, AU11, shows the least variability in tilt azimuth during each of the explosions. Changes in the characteristics of the regional deflationary signal source may also cause significant event-to-event variability in the observed tilts. As shown in Figure 2.4, even tilt fields generated by geometrically simple pressure sources can be complex and difficult to interpret when sparsely sampled.

We seek to invert for constraints on the source of the regional deflationary signal. In order to reduce the effect of local tilt sources on the regional deflation source estimates we select seven of the thirteen explosions to use for an inversion: 2, 3, 4, 6, 9, 11, and 13 (Fig. 4.2). We select events that best represent what we believe is a regional southwest trending tilt field that is present on a subset of the seismometers across all events.

Estimates of conduit dimensions and volume of eruptive products suggest that many of the explosive phase eruptions drained the conduit to a depth of approximately 2 km (Coombs *et al.*, 2010),
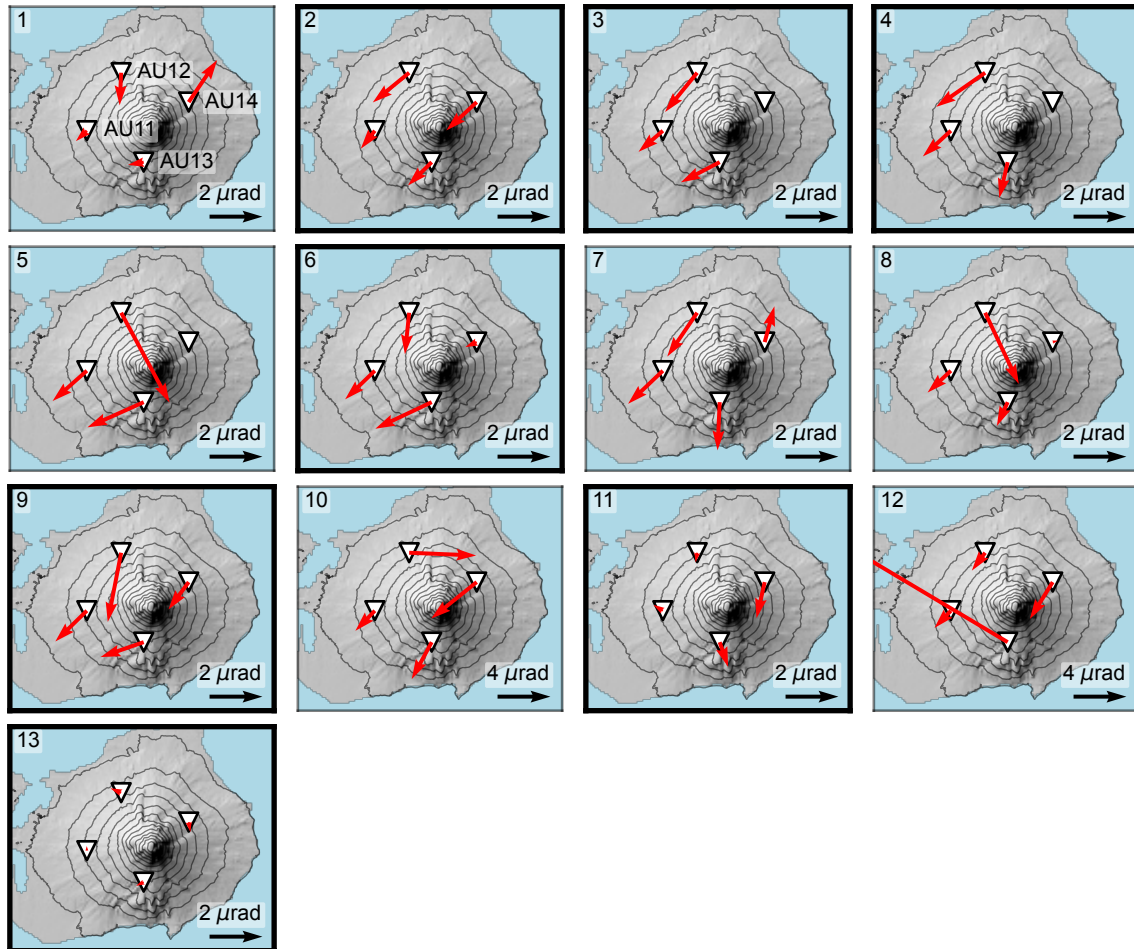
19

Figure 4.2: Tilt changes measured at each event during the explosive phase of the 2006 eruption of Augustine Volcano. The events are numbered in the upper left corner of each sub-panel according to Coombs *et al.* (2010). Tilt changes are measured as the difference between the tilt at the event time and a later measurement time within ten minutes of the event that is manually chosen per-event at the point of maximum monotonic tilt change. The vector for station AU13 in event 12 is intentionally left off-scale, as the seismometer experienced a tilt change of greater than 150 µrad. The events with bold borders are used in the deformation source inversion. Note different scales for events 10 and 12.

with the exception of the first two explosions on January 11, which contained little to no juvenile magma, and the final explosive sequence on January 27 and 28, which the authors believe tapped the deeper magma body. After each conduit-draining explosion the conduit is rapidly refilled by the volcano's magmatic system. Therefore, the regional tilt signal observed at each explosion on several minute timescales may contain deflation due to conduit depressurization during the initial explosion, in addition to deflation from a deeper source as the magmatic system below the volcano refills the conduit. The refilling conduit will lead to some amount of tilt "rebound", however the conduit likely does not return to its high pre-eruption pressure in the minutes following each explosion, so the net effect from the conduit remains deflationary. In our deformation model we utilize a deflating open conduit pinned to the surface (Nishimura, 2009) and a deflating prolate spheroid (Yang *et al.*, 1988) to represent the deeper magmatic system.

Independently inverting for a prolate spheroid and an open conduit deformation source for each event would lead to a very large number of free parameters, 13 per event, which is significantly more parameters than the eight tilt measurements (counting each horizontal seismometer component individually) that we have available for each event. Instead of inverting for the two unique deformation sources at each event, we jointly invert for many of the geometric parameters of the deformation sources using all events, and only allow the pressure change of the prolate spheroid, the pressure change of the open conduit, and the length of the open conduit to vary between events. The location and dimensions of the prolate spheroid and the location and radius of the open conduit are shared between all events. This leads to a total of 31 parameters in our inversion (10 shared plus 3 allowed to vary in each of 7 events) and 52, assumed independent, measurements. There is a data gap in the east-west horizontal channel of seismometer AU14 during events 3 and 4, so the AU14 measurements from events 3 and 4 are excluded from our analysis.

We perform probabilistic inversions of the observed tilt signals using VMOD analytical models (Angarita *et al.*, 2024) coupled with the emcee software package (Foreman-Mackey *et al.*, 2013), which implements a parallelized Markov Chain Monte Carlo ensemble sampler. For all analytical deformation models we use a 9.6 GPa shear modulus and a Poisson's ratio of 0.25. For our probabilistic inversion we use a Gaussian likelihood function with a 250 nrad standard deviation and prior distributions over each parameter that are uniform between the bounds listed in Table 4.1. We use 310 sampling chains (ten times the number of model parameters). Each chain is initialized in

21

Table 4.1: Bounds of uniform prior distributions over parameters used for the prolate spheroid source (top) and open conduit source (bottom) in the dual source inversion of tilt at Augustine Volcano. The x and y positions are relative to the EPSG:3338 coordinate (32305, 1040960), which is approximately the center of the summit of Augustine Volcano.

				Yang				
Param	X	Y	Depth	Semi-maj.	Semi-min.	Strike	Dip	ΔP
Unit	(km)	(km)	(km)	(km)	(km)	(deg)	(deg)	(MPa)
Low	-10	-10	1	0.05	0.05	0	0	-750
High	10	10	30	6	3	360	90	0

			Nishimura		
Param	X	Y	Radius	Length	ΔP
Unit	(km)	(km)	(m)	(km)	(MPa)
Low	-0.25	-0.25	0.1	0.1	-750
High	0.25	0.25	100	6	0

a small volume surrounding a reasonably well fitting set of parameters found with a coarse grid search and is allowed to run for 150,000 steps. The first 50,000 steps of each sampling chain are discarded as burn-in samples.

4.5 Discussion

Figure 4.3 shows the results of a probabilistic inversion for the deformation source parameters, Figure 4.4 is a diagram showing the median deformation source locations, and Figure 4.5 shows the median posterior tilt changes from the inversion result. We find a sub-vertical prolate spheroid south-southwest of the center of the volcano approximately 10 km below the surface and a depressurizing open conduit with a radius of approximately 16.5 m.

Our inversion shows that we are poorly sensitive to the parameters of the deflating open conduit source; many of the marginal distributions over the open conduit source parameters are broad, some even approaching the uniform prior distributions (Fig. 4.3). The seismometers used in this study are 1.5 km or more from the summit of Augustine Volcano, which places them in the far field of any shallow deformation source below the edifice. Figure 4.6b demonstrates this, the four seismometers are far enough from the source to be in regions of low tilt gradient, and are therefore much less sensitive to changes in the open conduit source than they are to changes in the prolate spheroid
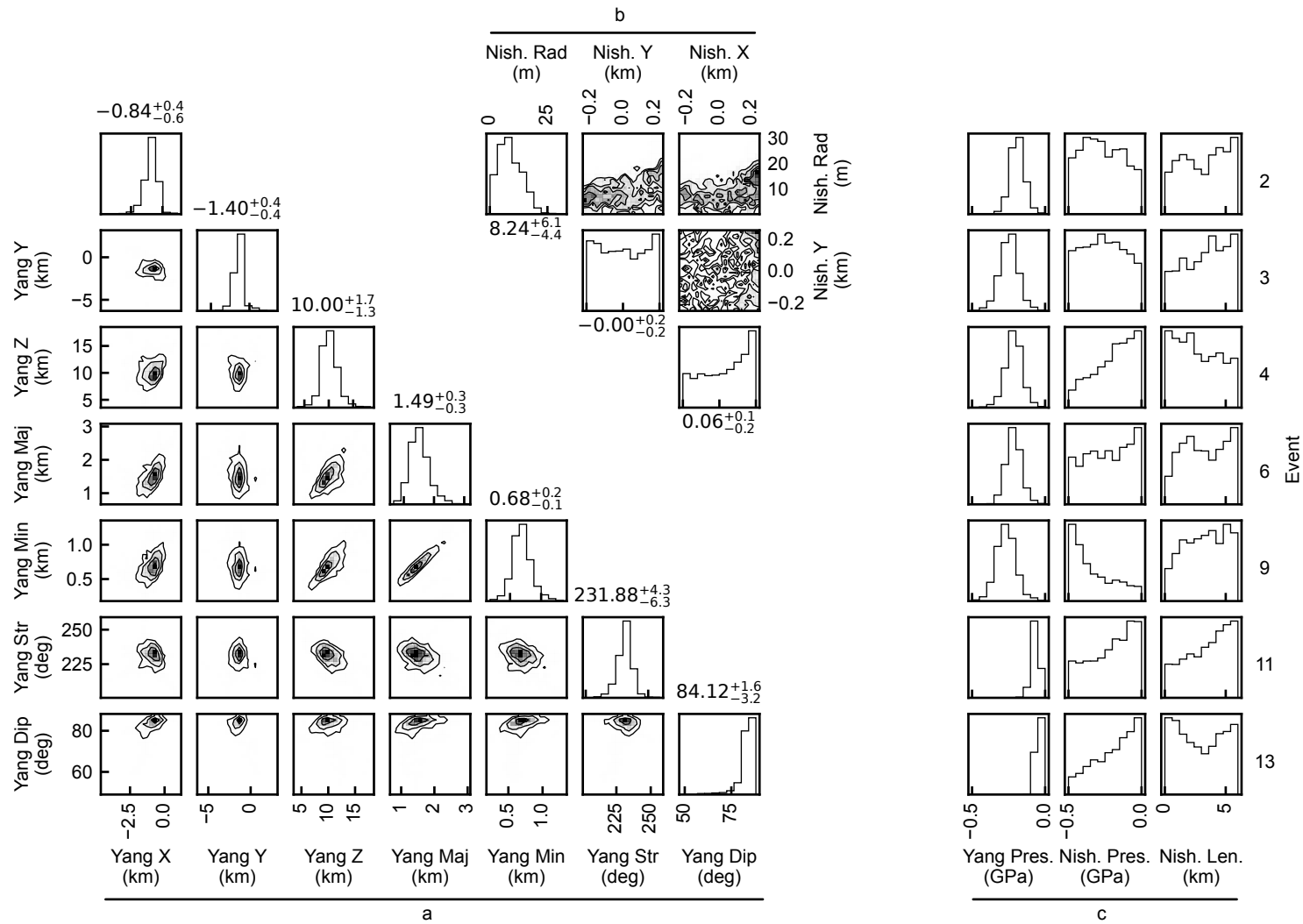
Figure 4.3: 2D histograms and marginal distributions of tilt source parameters in a dual deformation source inversion at Augustine Volcano using events 2, 3, 4, 6, 9, 11, and 13. **a)** Parameters describing location and geometry of the depressurizing prolate spheroid source model (Yang *et al.*, 1988), shared between all events. **b)** Parameters describing location and geometry of the depressurizing open conduit source model (Nishimura, 2009), shared between all events. **c)** Marginal distributions of per-event pressure changes for the two sources and the length of the depressurizing open conduit. The x position and y position parameter of each deformation source ("Yang X", "Yang Y", "Nish. X", "Nish. Y") are relative to the EPSG:3338 coordinate (32305, 1040960), which is approximately the center of the summit of Augustine Volcano. The number above each marginal distribution in panel sets a and b is the median value of the distribution, with the difference between the median value and the 16% quantile (bottom) and 84% quantile (top) to the right.
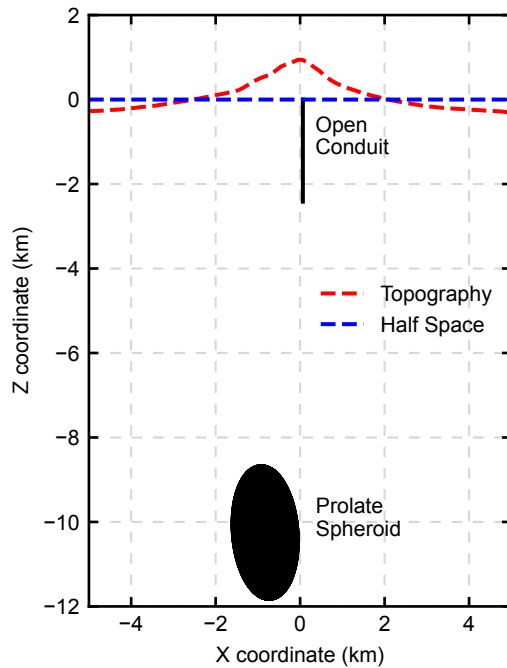
Figure 4.4: Diagram showing a cross section of inverted deflation source geometry at Augustine Volcano using the median parameter values given in Figure 4.3. The blue dashed line shows the top of the homogenous half space domain used in the tilt data inversion and the red dashed line shows the true topography of Augustine Volcano along the cross section. The diagram shows a projection of the two deformation sources onto an X-Z plane in the EPSG:3338 coordinate system (NAD83 / Alaska Albers) where the X coordinate is relative to the point (32305, 1040960) and the Z coordinate is relative to the surface of the homogenous half space used in the inversion.
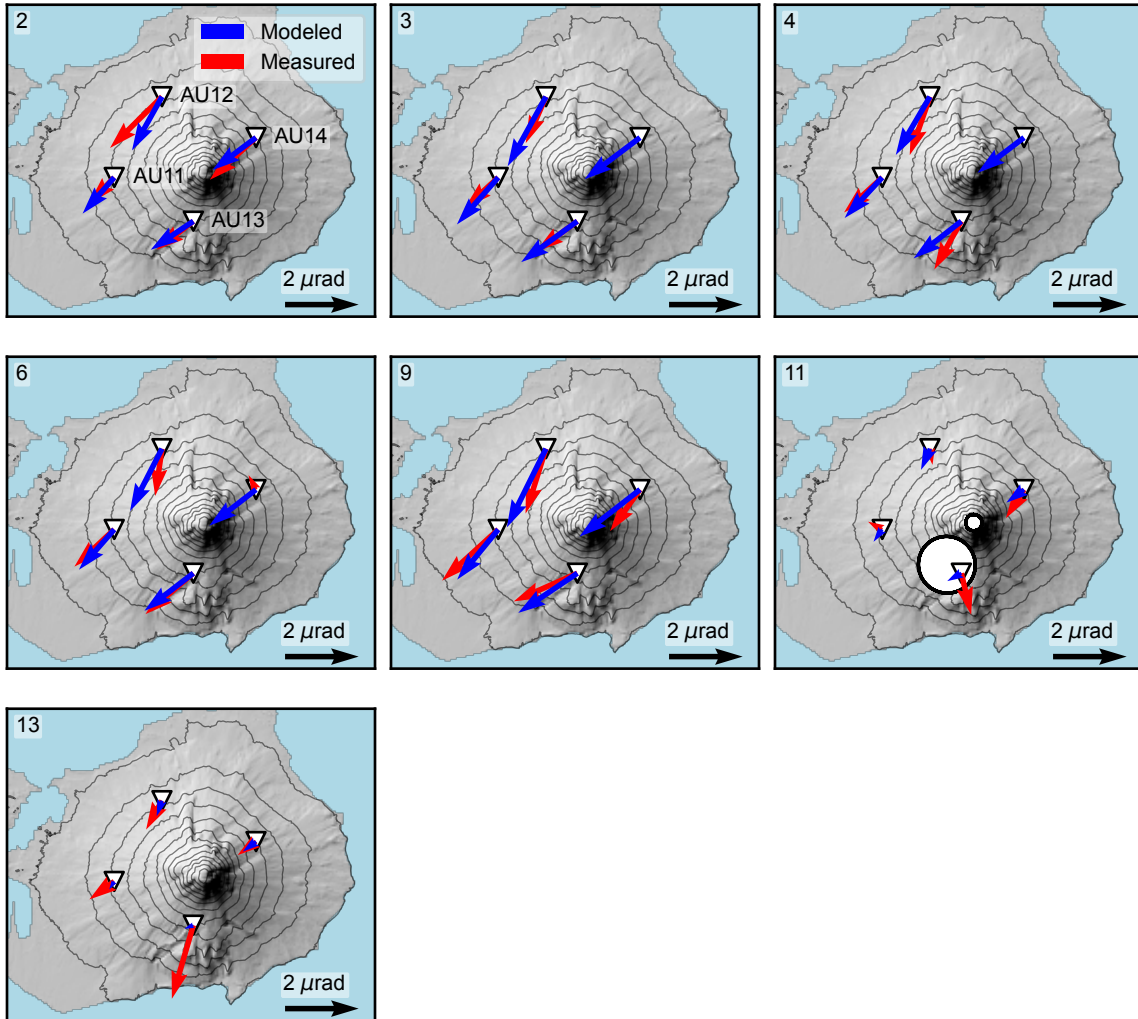
Figure 4.5: Maps of broadband seismometer-based tilt measurements from each of the seven explosions selected for use in the source inversion (red) and median modeled tilt from a prolate spheroid and open conduit pressure source pair using the results of the inversion (blue). The location and shape of the spheroid and and the location and radius of the open conduit are shared between all events, only the pressure change in each source and length of the conduit is allowed to vary between events. The white shapes with black outlines in the event 11 panel are the surface projections of the prolate spheroid source (larger) and the open conduit (smaller). The surface projection of the open conduit is larger than its true size for the purpose of visualization.

source. The open conduit source is necessary to achieve a reasonable inversion result, however. Figure A.1 shows the result of a tilt source inversion considering only a deflating prolate spheroid. The peak of the marginal distribution over prolate spheroid depth is at the edge of of the prior distribution over the parameter, 30 km, and the horizontal position of the spheroid is far from the edifice, outside of the seismometer network. Contribution from an open conduit source is necessary to fit the observed tilts well with the prolate spheroid at reasonable depths. Conversely, without a deeper, non-radially symmetric deformation source it would be impossible to fit the southwest trending tilt fields.

Petrologic studies of the products from the 2006 eruption of Augustine Volcano suggest that the magmatic system preceeding the eruption was made up of at least two physically separated magma reservoirs storing a low silica andesite and a high silica andesite at depths of 4-8 kilometers (Benage *et al.*, 2021; De Angelis *et al.*, 2013, 2020; Larsen *et al.*, 2010). This shallow storage system, which likely consists of a complex network of interconnected dikes (Roman *et al.*, 2006), was intruded by a basalt magma that heated and mobilized the low silica andesite. The mobilized low silica andesite forms the majority of the erupted material during explosive events 1-9 (Vallance *et al.*, 2010). Due to the approximately 10 km depth of our inverted deformation source, we believe that the deformation we observe is not caused by a net volume loss in the shallow (4-8 km depth) reservoir, but instead by the draw-up of either the intruding basalt magma or a deeper low silica andesite into the shallow reservoir following each explosion.

Cervelli *et al.* (2010) utilize GPS displacement measurements to invert for potential deformation sources during the effusive portion of Augustine Volcano's eruption, finding several potential depressurizing deformation sources that could explain the observed deformation; a spherical point source at 12.5 km depth, a 6 km long closed pipe with its center at 4.5 km depth, and a 4 km long open pipe with a center at 3.5 km depth. All sources are constrained to lie below the center of the edifice and only allowed to vary in size and depth. Cervelli *et al.* (2010) prefer the pipe models due to their shallower depths, which overlap with the petrologically constrained depths of the shallow reservoirs, but the shallower pipe models do not give a significantly better fit to the deformation data than the spherical source. Our explosive phase prolate spheroid deformation source overlaps in depth with the spherical deformation source and the lower portion of the closed pipe deformation source. This correspondence could be explained by both the explosive and effusive phases causing
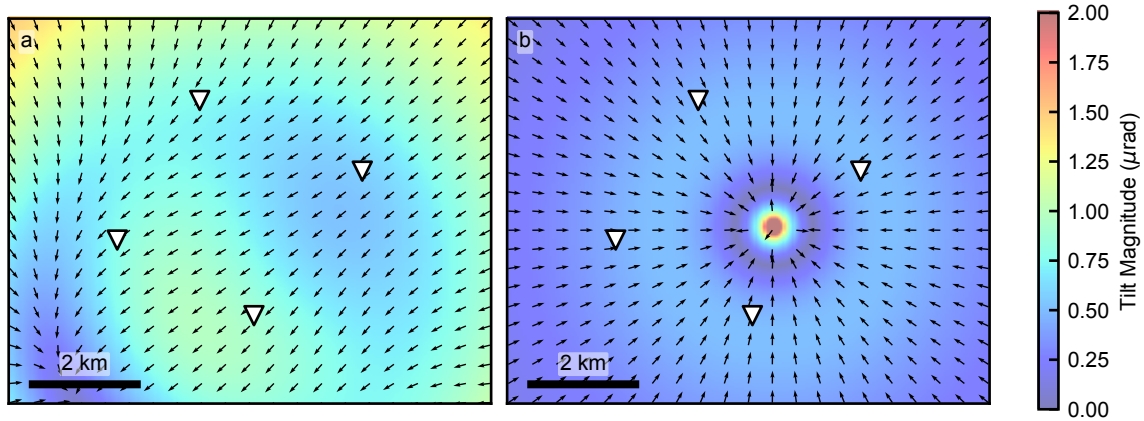
Figure 4.6: Example tilt fields caused by **a)** a sub-vertical de-pressurizing prolate spheroid source at approximately and **b)** a depressurizing open conduit source. Both tilt fields are generated using the median parameters from the dual tilt source inversion for event 4. The deeper prolate spheroid source affects a much larger area then the shallower open conduit source. The white triangles represent the relative positions of the seismometers on Augustine Volcano. The background color in each panel represents tilt magnitude, and the vectors tilt direction.

draw-up of the intruded basalt magma or deeper low silica andesite reservoir.

One issue with our inverted deformation sources are the volume changes of the prolate spheroid during each explosion. Each of the seven events we utilize for the dual deformation source inversion has a median posterior volume change of $10\text{-}80 \times 10^6 \, \text{m}^3$ (Fig. A.4). The total erupted volume during the thirteen explosive phase events is approximately $30 \times 10^6 \, \text{m}^3$ dense rock equivalent (DRE) (Coombs *et al.*, 2010). Such a large difference would not be expected if the evacuation of the upper conduit during each explosion was the dominant cause of the observed deformation signal. In our inversion we find that the deeper prolate spheroid deformation source, which we interpret as draw-up from a deeper magma reservoir in response to each explosion, is the dominant deformation source in most explosions. It may be reasonable then to observe total volume changes larger than the volume of erupted products if the drawn-up magma is not erupted during the explosive phase, or at all. Supporting this interpretation, there is poor correspondence between the volume of erupted material during the explosions and the observed tilt magnitudes. The first 9 explosions produced a total of $15.5 \times 10^6 \, \text{m}^3$ DRE of erupted material with an average tilt change of $1.61 \, \mu\text{rad}$ on each station during the explosions. The final 4 explosions (10-13) produced approximately the same amount of erupted material with an average tilt change of $1.19 \, \mu\text{rad}$ on each station (excluding a

150 μrad tilt change on a single seismometer during event 12).

Using the median geometric parameters from the seven event dual deformation source inversion (Fig. 4.4) we are able to invert for the per-event parameters (deformation source pressure changes and open conduit length) for all 13 explosions (Fig. A.3). In each case we find parameters that can reasonably explain the southwest trending tilt changes associated with each eruption, but fail to reproduce the larger event-to-event tilt changes that we believe are due to effects of mass flows.

Chapter 5: Conclusions

We have utilized broadband seismometers to observe ground tilt, allowing us to investigate the eruption dynamics of two different volcanic systems. At Mt. Erebus we demonstrate the absence of tilting associated with Strombolian eruptions, lending further support to the interpretation of Mt. Erebus as an end-member open vent magmatic system with a mechanically unobstructed upper conduit system that does not show any viscous plugging. At Augustine Volcano we find tilt deformation associated with explosions during the 2006 eruption. Our inversion of tilt measurements from a subset of individual explosions shows a good fit to a dual deflation source model with a depressurizing conduit above a deeper depressurizing prolate spheroid. This result is reasonably consistent with magma system models constrained by petrologic, seismic, visual, and GPS data.

Tilt measurements can capture ground deformation signals that are of smaller amplitude and shorter duration than what is possible with other geodetic techniques such as GNSS or InSAR. Our study has demonstrated the usefulness of broadband seismometer derived tilt as a tool to investigate small deformations occurring on timescales of minutes to hours. Additionally, we have demonstrated that broadband seismometer derived tilt can complement other geodetic observations and be used in a probabilistic inversion framework to make inferences about the magmatic plumbing of volcanoes using deformation signals from individual explosions.

Shorter period broadband seismometers (i.e., 30 or 60 s), such as those used at both Mt. Erebus and Augustine Volcano in this study, are well suited to make ground tilt measurements. An assumption of a tilt-dominated signal becomes defensible at periods of minutes or longer, allowing observation of small and transient deformation signals. Transitioning to longer period instruments (e.g. 240 or 360 s), while understandably desired by seismologists to increase quality of long period ground motion records, will lead to a loss of the ability to capture the minute to tens of minute period tilt signals that seismometer-derived tilt measurements are often used to observe. Tilt changes over the course of hours or days, such as what Wiens *et al.* (2005) measure at Anatahan Volcano, will still be observable, but tilting driven by changes in temperature and pressure or solid earth tides is significant at longer periods and increases the noise floor of the technique. For studies on volcanoes that seek to measure short-term transient tilt signals on timescales of minutes with broadband seismometers, it will be better to use shorter period instruments.

References

Ackerley, N. (2014) Principles of Broadband Seismometry. *Encyclopedia of Earthquake Engineering* (eds. M. Beer, I.A. Kougioumtzoglou, E. Patelli & I.S.K. Au), pp. 1–35, Springer Berlin Heidelberg.

Aderhold, K., Anderson, K.E., Reusch, A.M., Pfeifer, M.C., Aster, R.C. & Parker, T. (2015) Data Quality of Collocated Portable Broadband Seismometers Using Direct Burial and Vault Emplacement. *Bulletin of the Seismological Society of America* **105**, 2420–2432.

Agnew, D.C. (1986) Strainmeters and tiltmeters. *Reviews of Geophysics* **24**, 579–624.

Alaska Volcano Observatory/USGS (1988) Alaska Volcano Observatory. 10.7914/SN/AV.

Amoruso, A. & Crescentini, L. (2009) Shape and volume change of pressurized ellipsoidal cavities from deformation and seismic data. *Journal of Geophysical Research: Solid Earth* **114**.

Angarita, M., Grapenthin, R., Henderson, S., Christoffersen, M. & Anderson, K.R. (2024) Versatile Modeling Of Deformation (VMOD) Inversion Framework: Application to 20 Years of Observations at Westdahl Volcano and Fisher Caldera, Alaska, US. *Geochemistry, Geophysics, Geosystems* **25**, e2023GC011341.

Aster, R. (2003) Very long period oscillations of Mount Erebus Volcano. *Journal of Geophysical Research* **108**, 2522.

Battaglia, J., Aki, K. & Montagner, J.P. (2000) Tilt signals derived from a GEOSCOPE VBB Station on the Piton de la Fournaise Volcano. *Geophysical Research Letters* **27**, 605–608.

Benage, M.C., Wright, H.M.N. & Coombs, M.L. (2021) Eruption of compositionally heterogeneous andesites from a complex storage region during the 2006 eruption of Augustine Volcano. *Bulletin of Volcanology* **83**, 17.

Blick, G.H., Otway, P.M. & Scott, B.J. (1989) Deformation Monitoring of Mt. Erebus, Antarctica, 1980–1985. *Volcanic Hazards* (ed. J.H. Latter), pp. 554–560, Springer Berlin Heidelberg.

Capponi, A., Lane, S.J. & James, M.R. (2017) The implications of gas slug ascent in a stratified magma for acoustic and ground deformation source mechanisms in Strombolian eruptions. *Earth and Planetary Science Letters* **468**, 101–111.

Cervelli, P.F., Fournier, T.J., Freymueller, J.T., Power, J.A., Lisowski, M. & Pauk, B.A. (2010) Geodetic Constraints on Magma Movement and Withdrawal During the 2006 Eruption of Au-

gustine Volcano. *The 2006 eruption of Augustine Volcano, Alaska* (eds. J.A. Power, M.L. Coombs & J.T. Freymueller), vol. 1769.

Christoffersen, M. & Grapenthin, R. (2024) Seinei. 10.5281/zenodo.12709793.

Cooke, A. & Dricker, I. (2022) *evalresp - evaluate response information and output to ASCII files using rdseed V4.16 and above RESP files.* Seismological Facility for the Advancement of Geoscience.

Coombs, M.L., Bull, K.F., Vallance, J.W., Schneider, D.J., Thoms, E.E., Wessels, R.L. & McGimsey, R.G. (2010) Timing, Distribution, and Volume of Proximal Products of the 2006 Eruption of Augustine Volcano. *The 2006 eruption of Augustine Volcano, Alaska* (eds. J.A. Power, M.L. Coombs & J.T. Freymueller), vol. 1769.

Crozier, J., Karlstrom, L., Montgomery-Brown, E., Angarita, M., Cayol, V., Bato, M.G., Wang, T.A., Grapenthin, R., Shreve, T., Anderson, K., Astort, A., Bodart, O., Cannavò, F., Currenti, G., Dabaghi, F., Erickson, B.A., Garg, D., Head, M., Iozzia, A., Kim, Y.C., Le Mével, H., Novoa Lizama, C., Rucker, C., Silverii, F., Trasatti, E. & Zhan, Y. (2023) Understanding the drivers of volcano deformation through geodetic model verification and validation. *Bulletin of Volcanology* **85**, 74.

De Angelis, S.H., Larsen, J. & Coombs, M. (2013) Pre-eruptive Magmatic Conditions at Augustine Volcano, Alaska, 2006: Evidence from Amphibole Geochemistry and Textures. *Journal of Petrology* **54**, 1939–1961.

De Angelis, S.H., Larsen, J.F., Coombs, M.L., Utley, J.E.P. & Dunn, A. (2020) Phase equilibrium of a high-SiO$_2$ andesite at f$_{O_2}$ = RRO: implications for Augustine Volcano and other high-f$_{O_2}$ arc andesites. *Contributions to Mineralogy and Petrology* **175**, 24.

De Lauro, E., De Martino, S., Falanga, M. & Palo, M. (2009) Modelling the macroscopic behavior of Strombolian explosions at Erebus volcano. *Physics of the Earth and Planetary Interiors* **176**, 174–186.

Dibble, R.R., Kyle, P.R. & Rowe, C.A. (2008) Video and seismic observations of Strombolian eruptions at Erebus volcano, Antarctica. *Journal of Volcanology and Geothermal Research* **177**, 619–634.

Dzurisin, D. (2003) A comprehensive approach to monitoring volcano deformation as a window on the eruption cycle. *Reviews of Geophysics* **41**.

31

Dzurisin, D., Westphal, J.A. & Johnson, D.J. (1983) Eruption Prediction Aided by Electronic Tilt-meter Data at Mount St. Helens. *Science* **221**, 1381–1383.

Eaton, J.P. (1959) A portable water-tube tiltmeter. *Bulletin of the Seismological Society of America* **49**, 301–316.

Forbriger, T. (2007) Reducing magnetic field induced noise in broad-band seismic recordings. *Geophysical Journal International* **169**, 240–258.

Foreman-Mackey, D., Hogg, D.W., Lang, D. & Goodman, J. (2013) emcee: The MCMC Hammer. *Publications of the Astronomical Society of the Pacific* **125**, 306–312.

Foreman-Mackey, D., Price-Whelan, A., Vousden, W., Ryan, G., Pitkin, M., Zabalza, V., jsheyl, Smith, A., Ashton, G., Singer, L., Smith, M., Rice, E., Deline, A., Nitz, A., Brewer, B.J., Sipőcz, B., Hogg, D.W., Gentry, E., Rein, H., Madan, H., Czekala, I., NeutralKaon, Matthews, J., Tocknell, J., Barbary, K., Marlon, Prechelt, R., Hair, S.M.C. & Hoyer, S. (2023) dfm/corner.py: corner v2.2.2rc3.

Genco, R. & Ripepe, M. (2010) Inflation-deflation cycles revealed by tilt and seismic records at Stromboli volcano. *Geophysical Research Letters* **37**.

Gerst, A., Hort, M., Aster, R.C., Johnson, J.B. & Kyle, P.R. (2013) The first second of volcanic eruptions from the Erebus volcano lava lake, Antarctica—Energies, pressures, seismology, and infrasound. *Journal of Geophysical Research: Solid Earth* **118**, 3318–3340.

Giggenbach, W.F., Kyle, P.R. & Lyon, G.L. (1973) Present Volcanic Activity on Mount Erebus, Ross Island, Antarctica. *Geology* **1**, 135–136.

Graizer, V. (2006) Tilts in Strong Ground Motion. *Bulletin of the Seismological Society of America* **96**, 2090–2102.

Graizer, V. (2009) The Response to Complex Ground Motions of Seismometers with Galperin Sensor Configuration. *Bulletin of the Seismological Society of America* **99**, 1366–1377.

Grapenthin, R., Kyle, P., Aster, R.C., Angarita, M., Wilson, T. & Chaput, J. (2022) Deformation at the open-vent Erebus volcano, Antarctica, from more than 20 years of GNSS observations. *Journal of Volcanology and Geothermal Research* **432**, 107703.

Grapenthin, R., Ófeigsson, B.G., Sigmundsson, F., Sturkell, E. & Hooper, A. (2010) Pressure sources versus surface loads: Analyzing volcano deformation signal composition with an application to Hekla volcano, Iceland. *Geophysical Research Letters* **37**.

Harris, C.R., Millman, K.J., Van Der Walt, S.J., Gommers, R., Virtanen, P., Cournapeau, D., Wieser, E., Taylor, J., Berg, S., Smith, N.J., Kern, R., Picus, M., Hoyer, S., Van Kerkwijk, M.H., Brett, M., Haldane, A., Del Río, J.F., Wiebe, M., Peterson, P., Gérard-Marchant, P., Sheppard, K., Reddy, T., Weckesser, W., Abbasi, H., Gohlke, C. & Oliphant, T.E. (2020) Array programming with NumPy. *Nature* **585**, 357–362.

Harrison, J.C. (1976) Cavity and topographic effects in tilt and strain measurement. *Journal of Geophysical Research (1896-1977)* **81**, 319–328.

Hunter, J.D. (2007) Matplotlib: A 2D graphics environment. *Computing in Science & Engineering* **9**, 90–95.

Iguchi, M., Yakiwara, H., Tameguri, T., Hendrasto, M. & Hirabayashi, J.i. (2008) Mechanism of explosive eruption revealed by geophysical observations at the Sakurajima, Suwanosejima and Semeru volcanoes. *Journal of Volcanology and Geothermal Research* **178**, 1–9.

Jaggar, T.A. (1920) Seismometric investigation of the Hawaiian lava column. *Bulletin of the Seismological Society of America* **10**, 155–275.

Jaggar, T.A. & Finch, R.H. (1929) Tilt records for thirteen years at the Hawaiian Volcano Observatory. *Bulletin of the Seismological Society of America* **19**, 38–51.

James, M.R., Lane, S.J. & Chouet, B.A. (2006) Gas slug ascent through changes in conduit diameter: Laboratory insights into a volcano-seismic source process in low-viscosity magmas. *Journal of Geophysical Research: Solid Earth* **111**.

Jones, L.K., Kyle, P.R., Oppenheimer, C., Frechette, J.D. & Okal, M.H. (2015) Terrestrial laser scanning observations of geomorphic changes and varying lava lake levels at Erebus volcano, Antarctica. *Journal of Volcanology and Geothermal Research* **295**, 43–54.

Klein, F.W. (1984) Eruption forecasting at Kilauea Volcano, Hawaii. *Journal of Geophysical Research: Solid Earth* **89**, 3059–3073.

Knox, H.A., Chaput, J.A., Aster, R.C. & Kyle, P.R. (2018) Multiyear Shallow Conduit Changes Observed With Lava Lake Eruption Seismograms at Erebus Volcano, Antarctica. *Journal of Geophysical Research: Solid Earth* **123**, 3178–3196.

Kuswandarto, H., Hendrasto, M. & Iguchi, M. (2008) Automatic and Real-time Processing of Tilt Records for Prediction of Explosions at Semeru Volcano, East Java, Indonesia. *Indonesian Journal of Physics* **19**, 69–74.

Larsen, J.F., Nye, C.J., Coombs, M.L., Tilman, M., Izbekov, P. & Cameron, C. (2010) Petrology and Geochemistry of the 2006 Eruption of Augustine Volcano. *The 2006 eruption of Augustine Volcano, Alaska* (eds. J.A. Power, M.L. Coombs & J.T. Freymueller), vol. 1769.

Lyons, J.J., Waite, G.P., Ichihara, M. & Lees, J.M. (2012) Tilt prior to explosions and the effect of topography on ultra-long-period seismic records at Fuego volcano, Guatemala. *Geophysical Research Letters* **39**.

Marsden, L.H., Neuberg, J.W. & Thomas, M.E. (2019) Topography and Tilt at Volcanoes. *Frontiers in Earth Science* **7**.

Mattia, M., Palano, M., Aloisi, M., Bruno, V. & Bock, Y. (2008) High rate GPS data on active volcanoes: an application to the 2005–2006 Mt. Augustine (Alaska, USA) eruption. *Terra Nova* **20**, 134–140.

McKee, K.F., Roman, D.C., Waite, G.P. & Fee, D. (2022) Silent Very Long Period Seismic Events (VLPs) at Stromboli Volcano, Italy. *Geophysical Research Letters* **49**.

McKinney, W. (2010) Data Structures for Statistical Computing in Python. *Proceedings of the 9th Python in Science Conference* (eds. S.v.d. Walt & J. Millman), pp. 56 – 61.

Nishimura, T. (2009) Ground deformation caused by magma ascent in an open conduit. *Journal of Volcanology and Geothermal Research* **187**, 178–192.

ObsPy Development Team (2022) ObsPy 1.4.0. 10.5281/zenodo.6645832.

Odbert, H., Taisne, B. & Gottsmann, J. (2015) Deposit loading and its effect on co-eruptive volcano deformation. *Earth and Planetary Science Letters* **413**, 186–196.

pandas Development Team (2020) pandas v2.2.2. 10.5281/zenodo.3509134.

Power, J.A., Coombs, M.L. & Freymueller, J.T. (eds.) (2010) *The 2006 eruption of Augustine Volcano, Alaska: U.S. Geological Survey Professional Paper 1769*. 1 plate, scale 1:20,000, and data files.

Ringler, A.T. & Bastien, P. (2020) A Brief Introduction to Seismic Instrumentation: Where Does My Data Come From? *Seismological Research Letters* **91**, 1074–1083.

Ripepe, M. & Marchetti, E. (2002) Array tracking of infrasonic sources at Stromboli volcano. *Geophysical Research Letters* **29**.

Roman, D.C., Cashman, K.V., Gardner, C.A., Wallace, P.J. & Donovan, J.J. (2006) Storage and interaction of compositionally heterogeneous magmas from the 1986 eruption of Augustine Vol-

cano, Alaska. *Bulletin of Volcanology* **68**, 240–254.

Rowe, C.A., Aster, R.C., Kyle, P.R., Dibble, R.R. & Schlue, J.W. (2000) Seismic and acoustic observations at Mount Erebus Volcano, Ross Island, Antarctica, 1994–1998. *Journal of Volcanology and Geothermal Research* **101**, 105–128.

Tape, C., Ringler, A.T. & Hampton, D.L. (2020) Recording the Aurora at Seismometers across Alaska. *Seismological Research Letters* **91**, 3039–3053.

Vallance, J.W., Bull, K.F. & Coombs, M.L. (2010) Pyroclastic Flows, Lahars, and Mixed Avalanches Generated During the 2006 Eruption of Augustine Volcano. *The 2006 eruption of Augustine Volcano, Alaska* (eds. J.A. Power, M.L. Coombs & J.T. Freymueller), vol. 1769.

Virtanen, P., Gommers, R., Oliphant, T.E., Haberland, M., Reddy, T., Cournapeau, D., Burovski, E., Peterson, P., Weckesser, W., Bright, J., Van Der Walt, S.J., Brett, M., Wilson, J., Millman, K.J., Mayorov, N., Nelson, A.R.J., Jones, E., Kern, R., Larson, E., Carey, C.J., Polat, I., Feng, Y., Moore, E.W., VanderPlas, J., Laxalde, D., Perktold, J., Cimrman, R., Henriksen, I., Quintero, E.A., Harris, C.R., Archibald, A.M., Ribeiro, A.H., Pedregosa, F., Van Mulbregt, P., SciPy 1.0 Contributors, Vijaykumar, A., Bardelli, A.P., Rothberg, A., Hilboll, A., Kloeckner, A., Scopatz, A., Lee, A., Rokem, A., Woods, C.N., Fulton, C., Masson, C., Häggström, C., Fitzgerald, C., Nicholson, D.A., Hagen, D.R., Pasechnik, D.V., Olivetti, E., Martin, E., Wieser, E., Silva, F., Lenders, F., Wilhelm, F., Young, G., Price, G.A., Ingold, G.L., Allen, G.E., Lee, G.R., Audren, H., Probst, I., Dietrich, J.P., Silterra, J., Webber, J.T., Slavič, J., Nothman, J., Buchner, J., Kulick, J., Schönberger, J.L., De Miranda Cardoso, J.V., Reimer, J., Harrington, J., Rodríguez, J.L.C., Nunez-Iglesias, J., Kuczynski, J., Tritz, K., Thoma, M., Newville, M., Kümmerer, M., Bolingbroke, M., Tartre, M., Pak, M., Smith, N.J., Nowaczyk, N., Shebanov, N., Pavlyk, O., Brodtkorb, P.A., Lee, P., McGibbon, R.T., Feldbauer, R., Lewis, S., Tygier, S., Sievert, S., Vigna, S., Peterson, S., More, S., Pudlik, T., Oshima, T., Pingel, T.J., Robitaille, T.P., Spura, T., Jones, T.R., Cera, T., Leslie, T., Zito, T., Krauss, T., Upadhyay, U., Halchenko, Y.O. & Vázquez-Baeza, Y. (2020) SciPy 1.0: fundamental algorithms for scientific computing in Python. *Nature Methods* **17**, 261–272.

Welch, P. (1967) The use of fast Fourier transform for the estimation of power spectra: A method based on time averaging over short, modified periodograms. *IEEE Transactions on Audio and Electroacoustics* **15**, 70–73.

Wenner, M., Allstadt, K., Thelen, W., Lockhart, A., Hirschberg, J., McArdell, B.W. & Walter, F. (2022) Seismometer Records of Ground Tilt Induced by Debris Flows. *Bulletin of the Seismological Society of America* **112**, 2376–2395.

Westphal, J.A., Carr, M.A., Miller, W.F. & Dzurisin, D. (1983) Expendable bubble tiltmeter for geophysical monitoring. *Review of Scientific Instruments* **54**, 415–418.

Wielandt, E. & Forbriger, T. (1999) Near-field seismic displacement and tilt associated with the explosive activity of Stromboli. *Annali Di Geofisica* **42**, 407–416.

Wiens, D.A., Pozgay, S.H., Shore, P.J., Sauter, A.W. & White, R.A. (2005) Tilt recorded by a portable broadband seismograph: The 2003 eruption of Anatahan Volcano, Mariana Islands. *Geophysical Research Letters* **32**.

Wilson, C.R. (2021) *Essentials of geophysical data processing*. Cambridge University Press, Cambridge, England.

Wright, R. (2016) MODVOLC: 14 years of autonomous observations of effusive volcanism from space. *Detecting, Modelling and Responding to Effusive Eruptions*, Geological Society of London.

Yang, X.M., Davis, P.M. & Dieterich, J.H. (1988) Deformation from inflation of a dipping finite prolate spheroid in an elastic half-space as a model for volcanic stressing. *Journal of Geophysical Research: Solid Earth* **93**, 4249–4257.

Zandomeneghi, D., Aster, R., Kyle, P., Barclay, A., Chaput, J. & Knox, H. (2013) Internal structure of Erebus volcano, Antarctica imaged by high-resolution active-source seismic tomography and coda interferometry. *Journal of Geophysical Research: Solid Earth* **118**, 1067–1078.
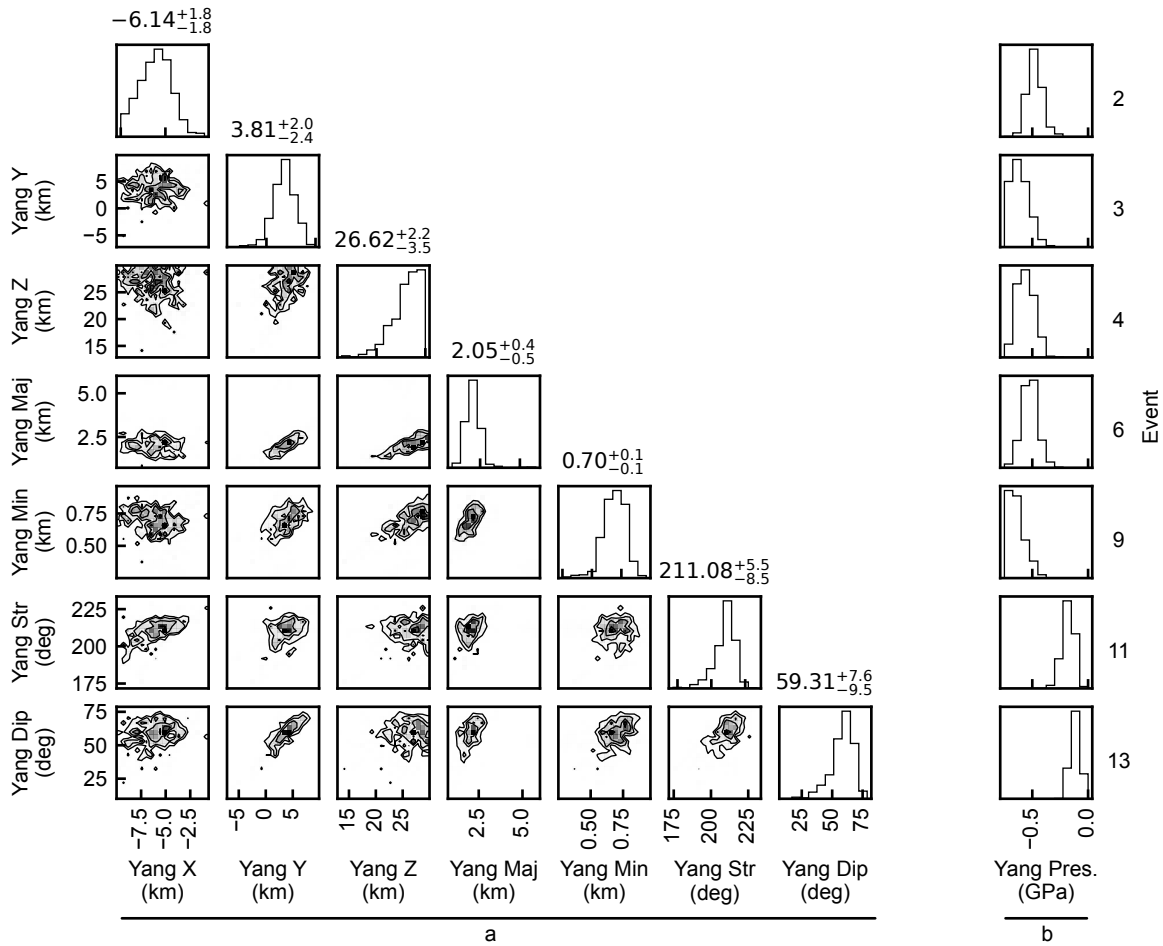
Figure A.1: 2D histograms and marginal distributions of tilt source parameters in a single deformation source inversion at Augustine Volcano using events 2, 3, 4, 6, 9, 11, and 13. **a)** Parameters describing location and geometry of the depressurizing prolate spheroid source model (Yang *et al.*, 1988), shared between all events. **b)** Marginal distributions of per-event pressure changes for the prolate spheroid source. The x position and y position parameter of the deformation source ("Yang X", "Yang Y") are relative to the EPSG:3338 coordinate (32305, 1040960), which is approximately the center of the summit of Augustine Volcano. The number above each marginal distribution in panel set a is the median value of the distribution, with the difference between the median value and the 16% quantile (bottom) and 84% quantile (top) to the right.
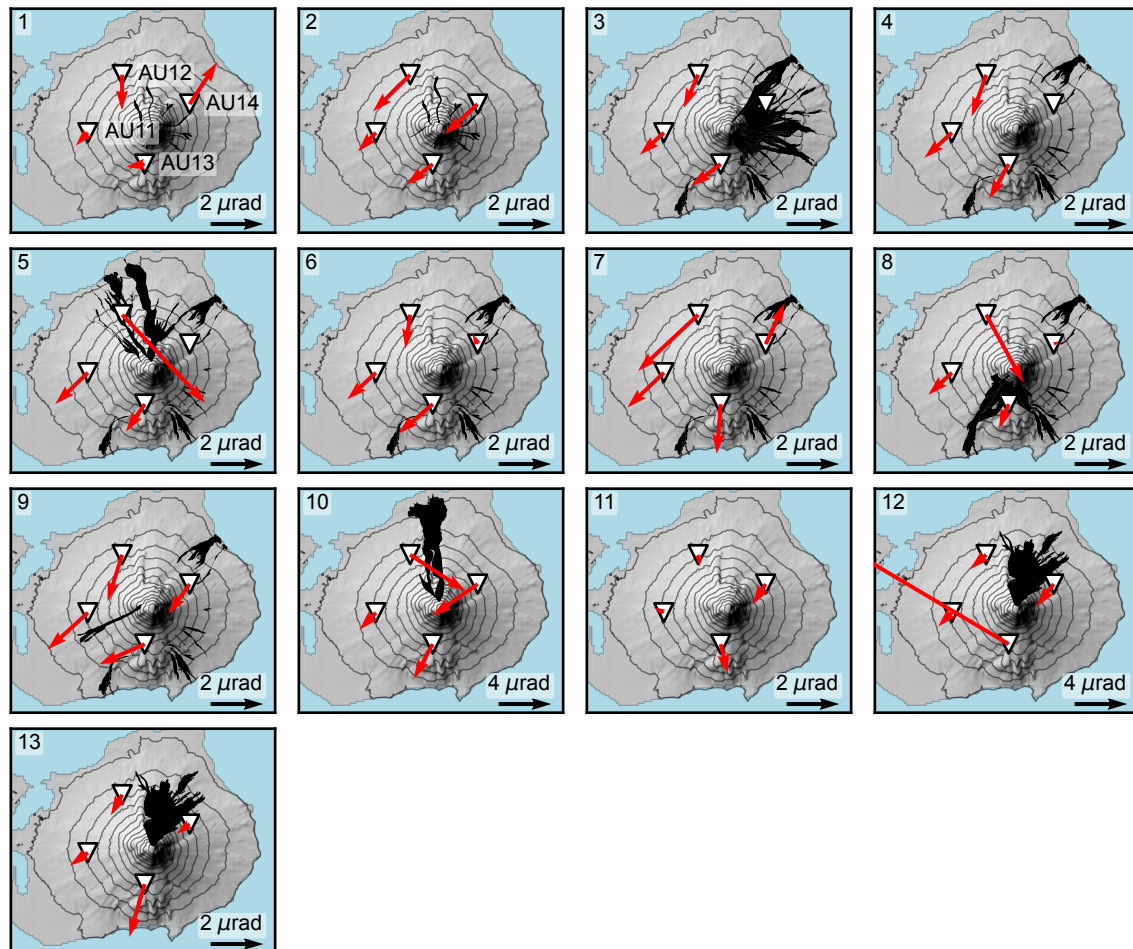
Figure A.2: Locations of mass flows (avalanches, lahars, and pyroclastic flows) at Augustine Volcano (black) mapped by Coombs *et al.* (2010) and tilt changes associated with each explosion during the 2006 eruption (red arrows). Each mass flow is plotted with the event that generated it. When there is uncertainty about the exact event that generated a mass flow it is plotted with all events that may have generated it. There is some correlation between mass flows and spurious tilts observed on broadband seismometers (e.g., AU12 during event 5, AU14 during event 7, and AU12 during event 10), however not all mass flows emplaced near seismometers cause spurious tilt, and not all spurious tilts are associated with mass flows mapped by Coombs *et al.* (2010).
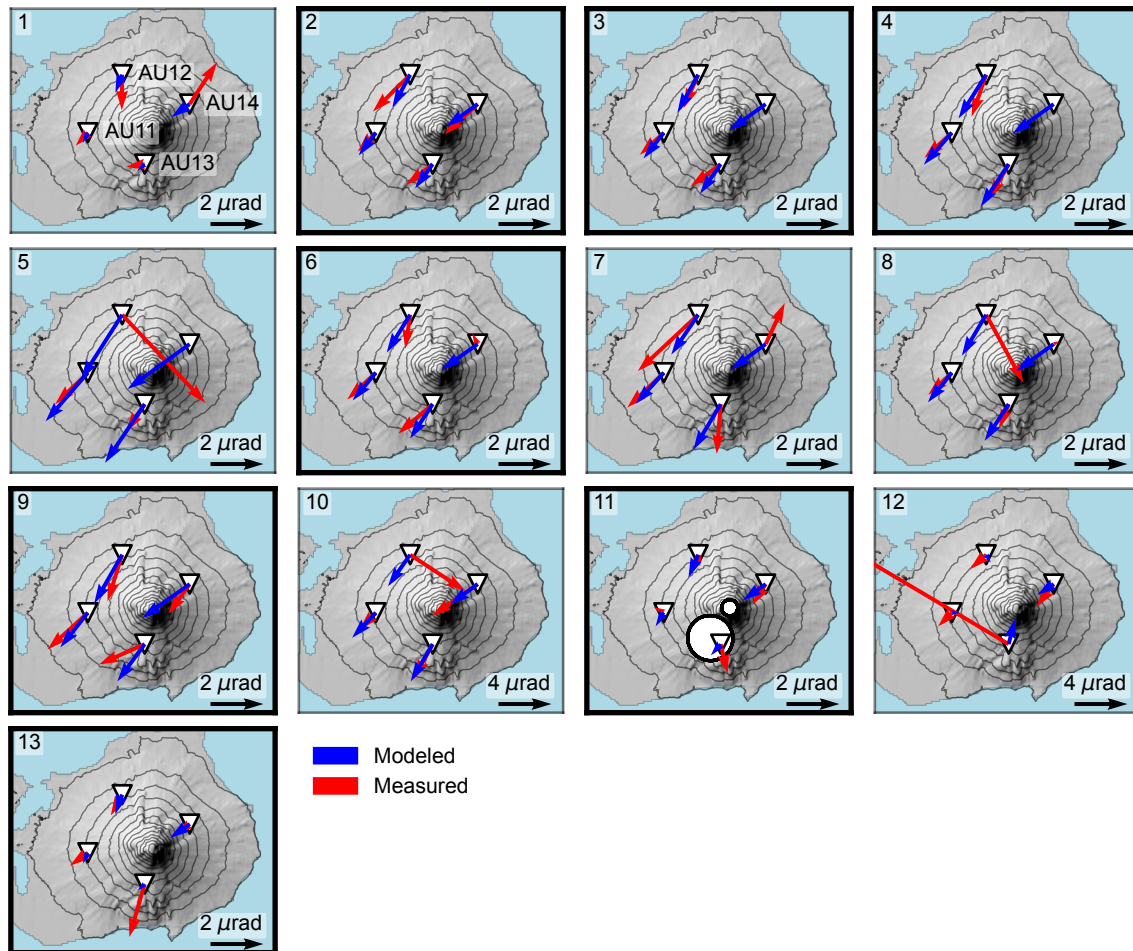
Figure A.3: Maps of broadband seismometer-based tilt measurements from each of the thirteen explosions during the explosive phase of the 2006 eruption of Augustine Volcano (red) and modeled tilt from a prolate spheroid and open conduit pressure source pair that are fixed to the median geometric parameters from the dual deformation source inversion using a subset of the explosions (Figure 4.3 panel sets a and b) (blue). The pressure change of each source and the length of the open conduit source are inverted for each event, and we plot the median posterior tilt in each case. The events with bold borders are used in the dual deformation source inversion using a subset of the explosions.
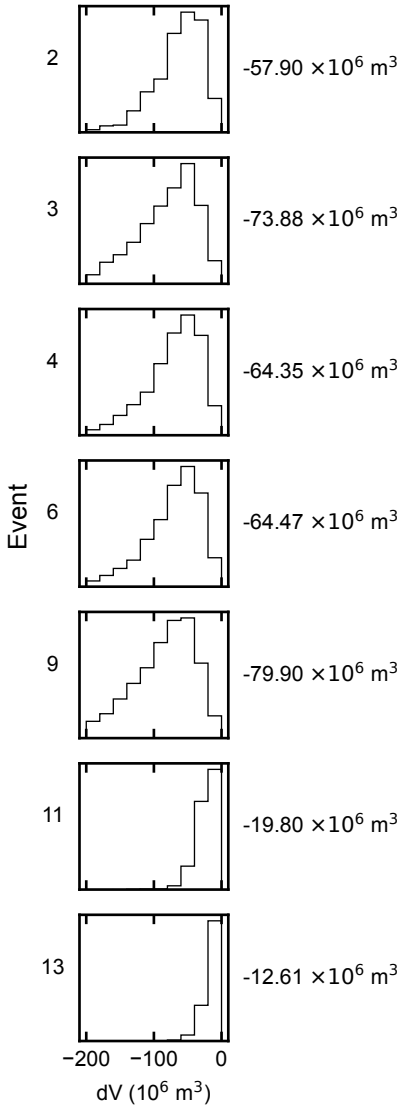
Figure A.4: Posterior distributions of prolate spheroid volume changes for each event used in the deformation source inversion at Augustine Volcano. Volume changes are calculated using the method of Amoruso & Crescentini (2009). The median volume change values (to the right of each panel) are large compared to the total erupted volume during the explosive phase, however we believe the deformation we observe is only caused in part by the evacuation of the upper conduit of Augustine Volcano during each explosion and that the bulk of the deformation signal comes from mobilization of magma in a deeper reservoir, which may experience volume changes that are significantly different than the volume of erupted material.

Event 1

Event 2

Event 3

Event 4

42

Event 7
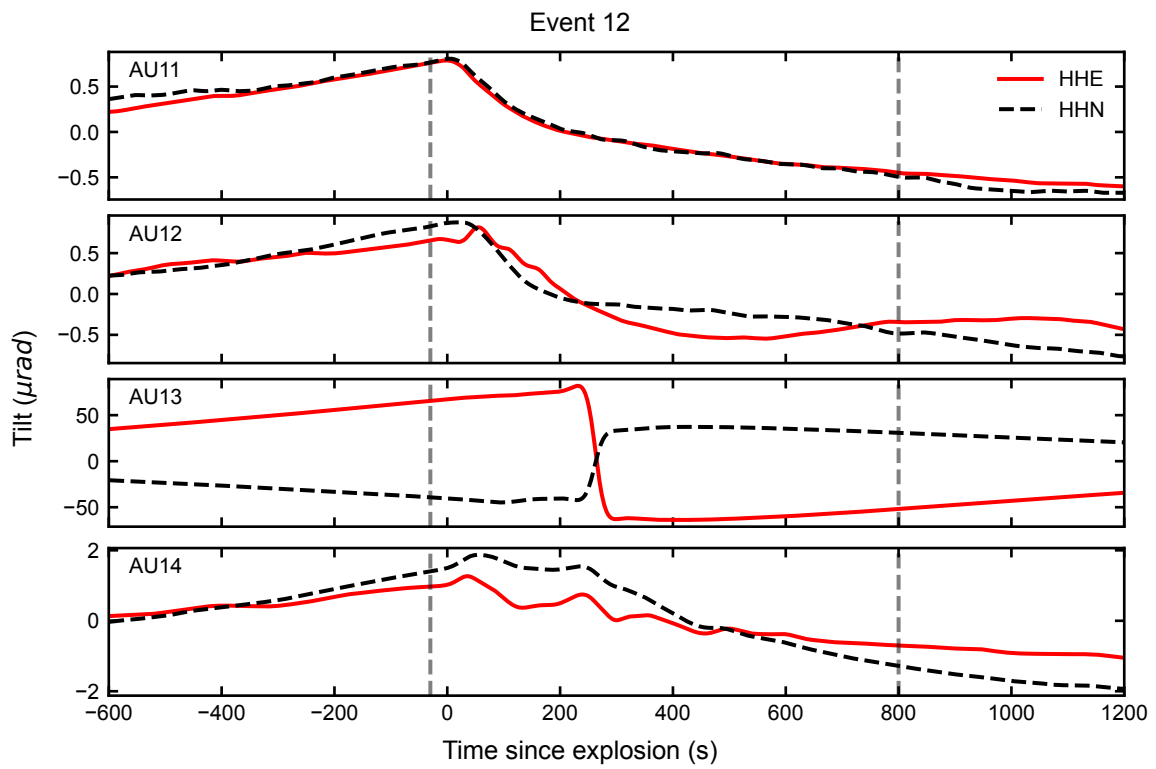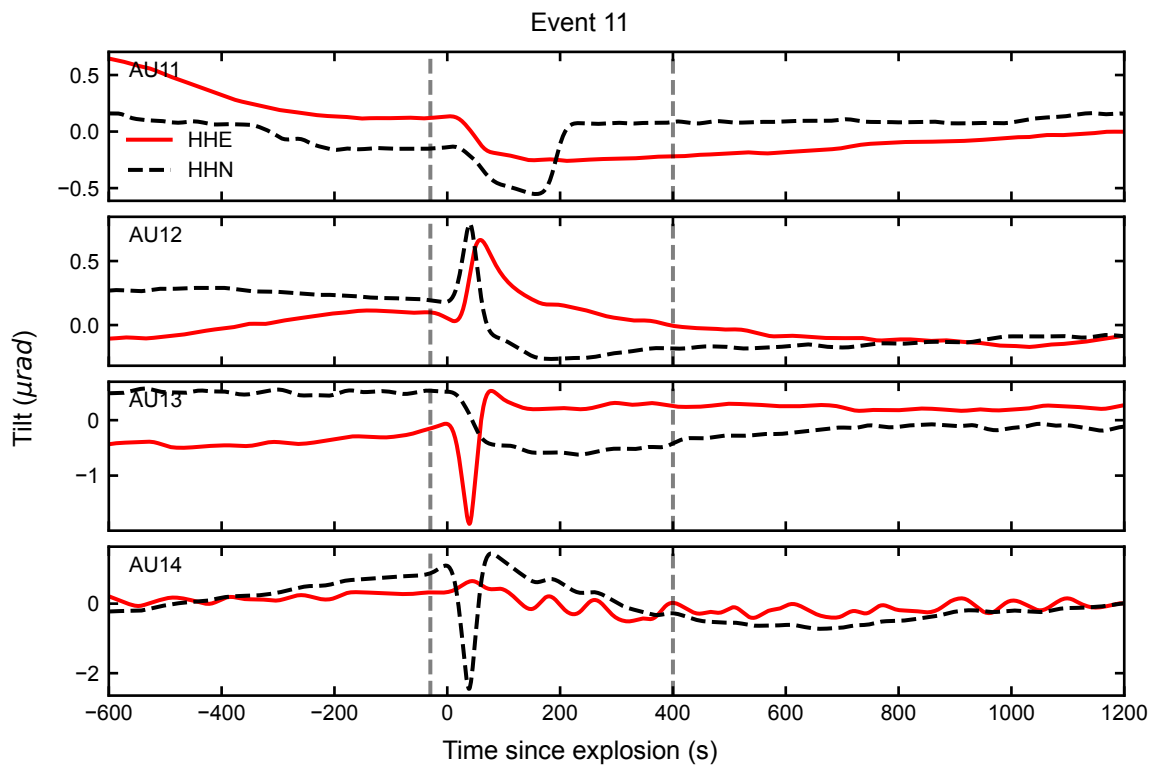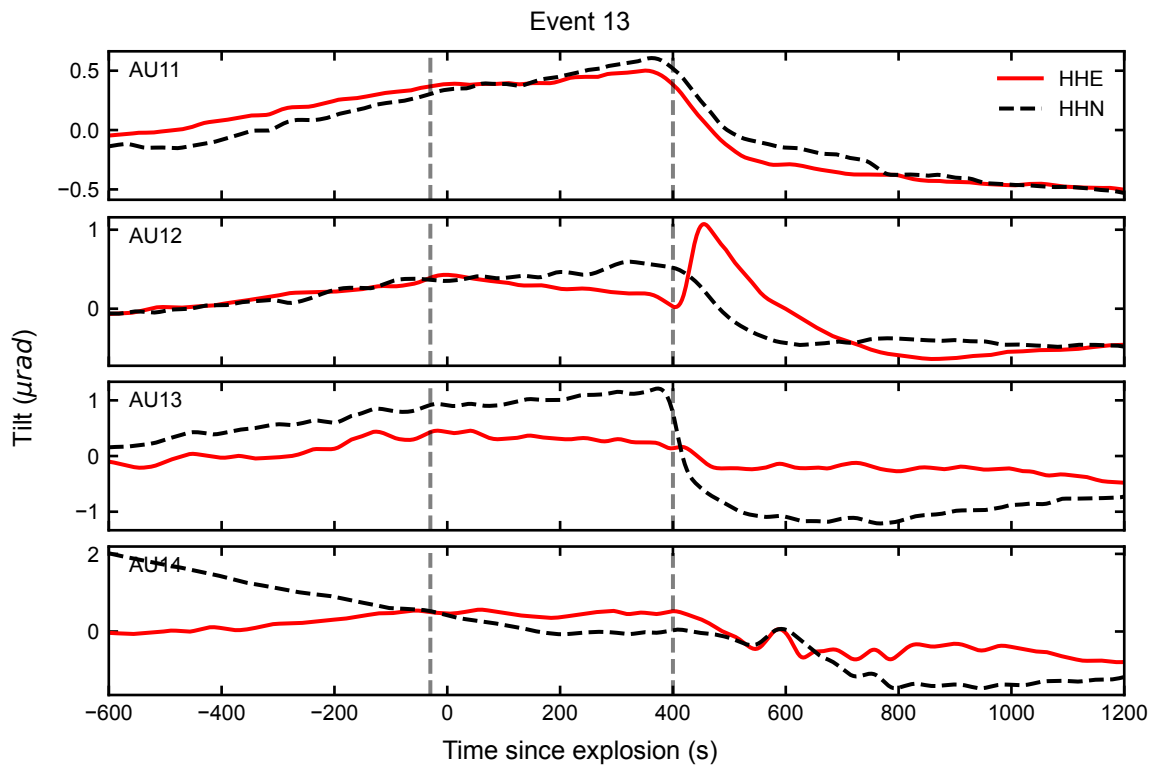
Event 8

Event 11

Event 12
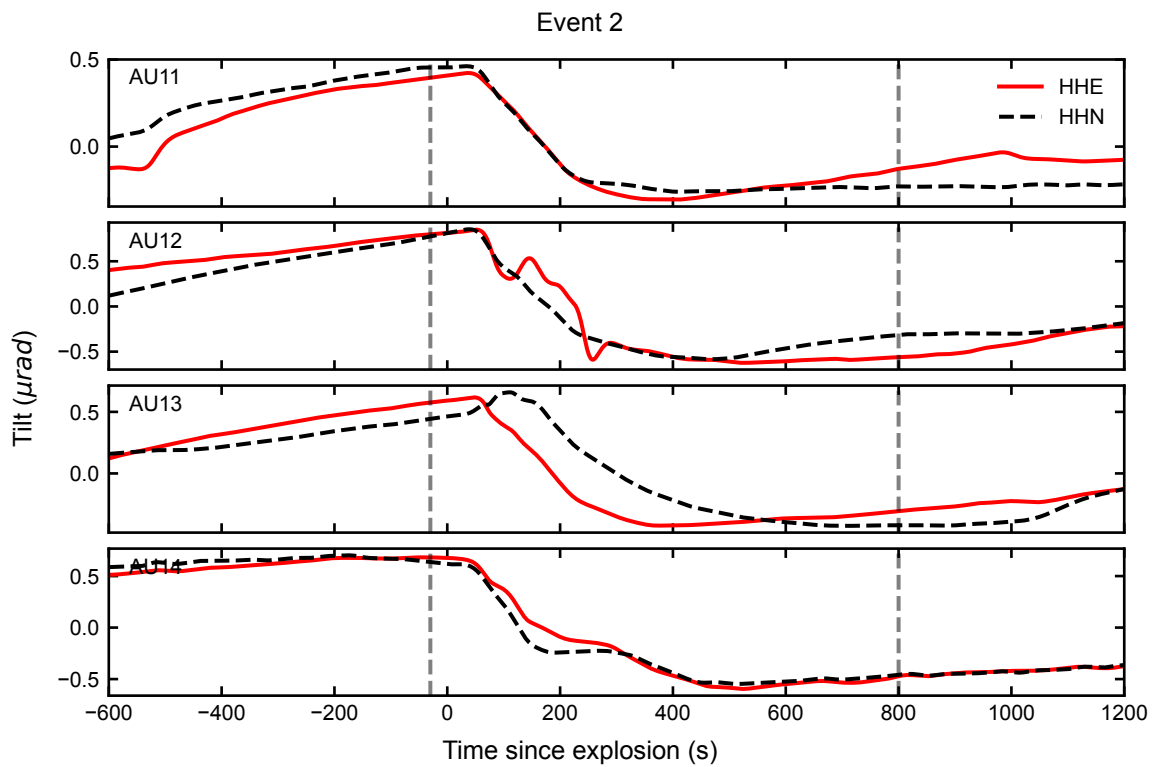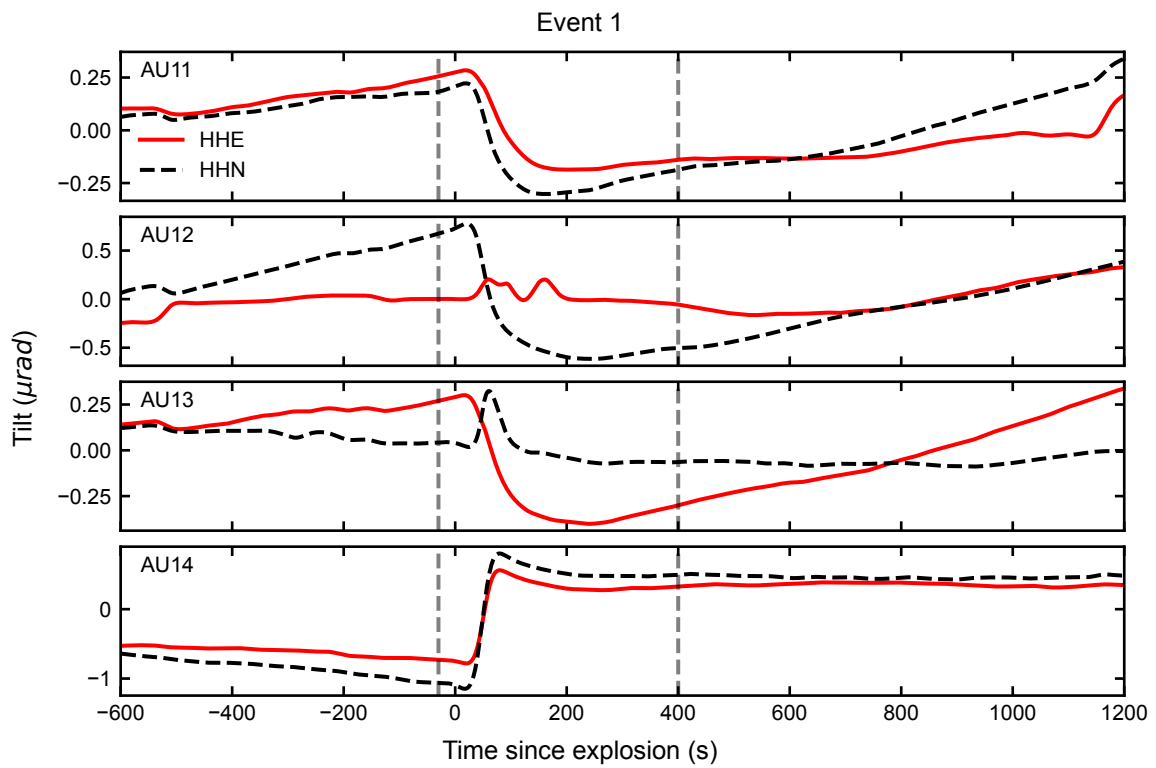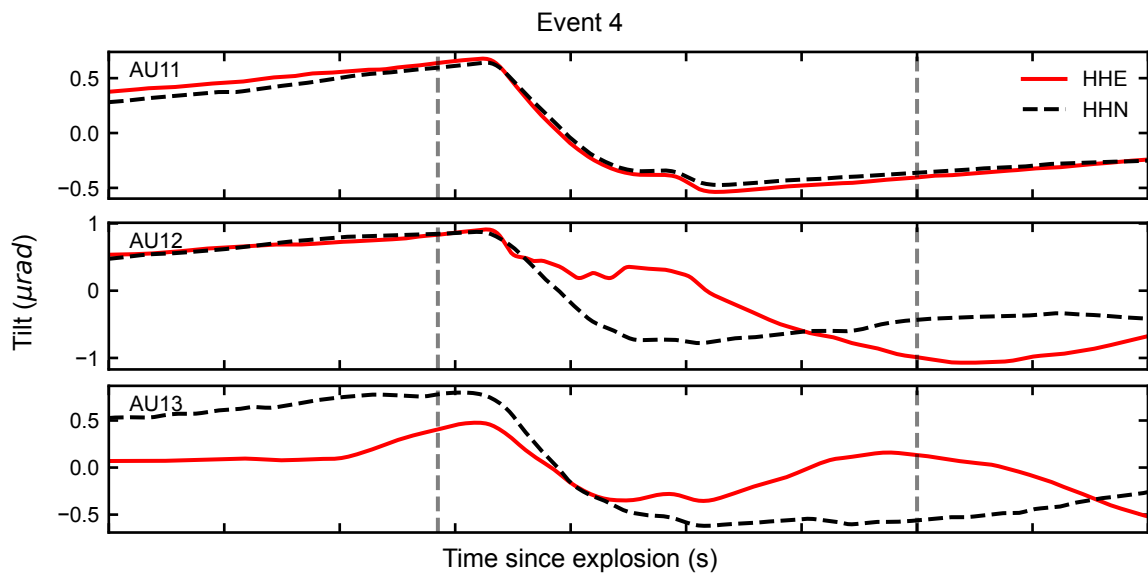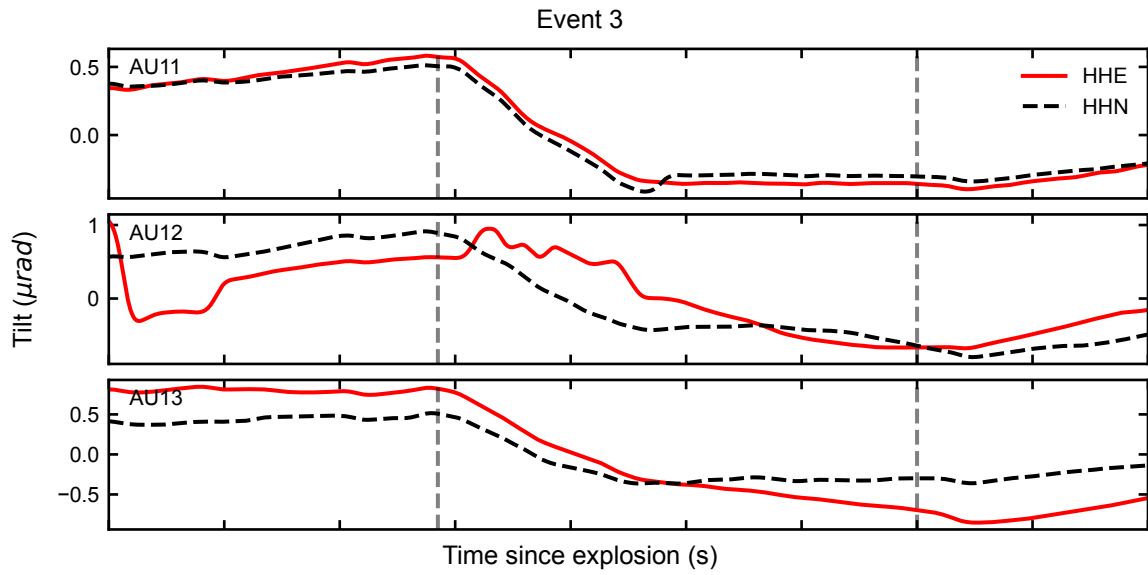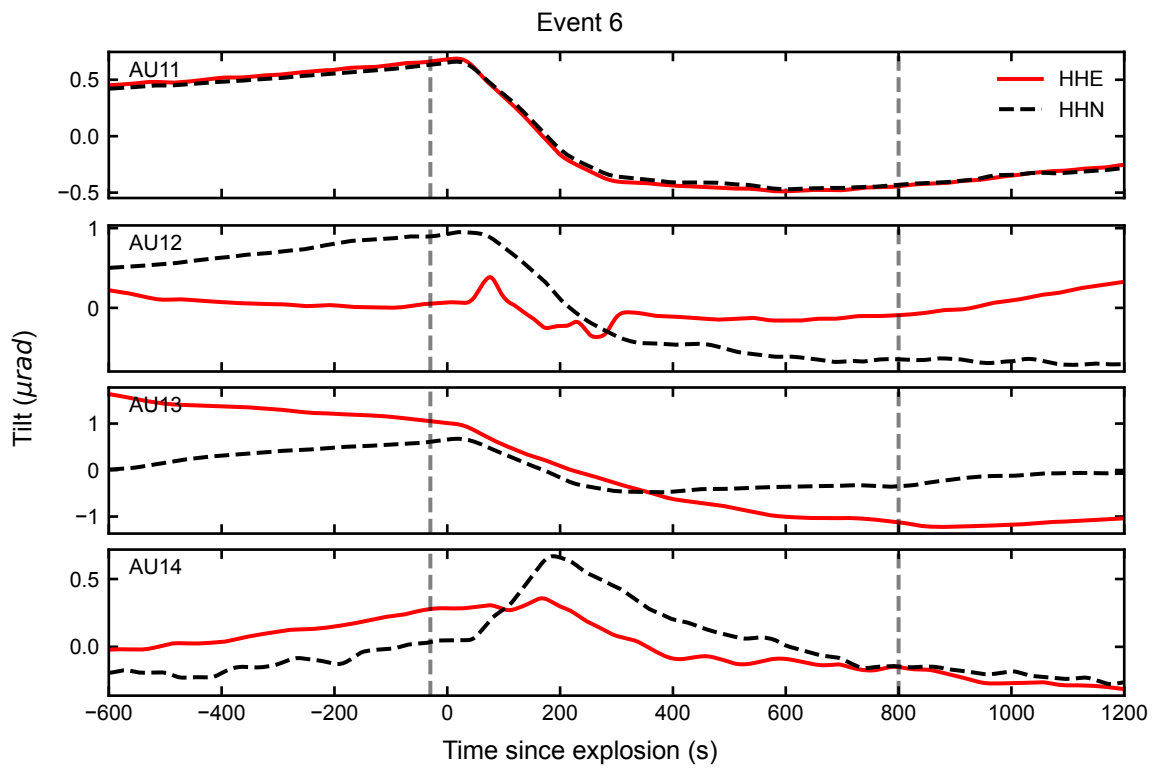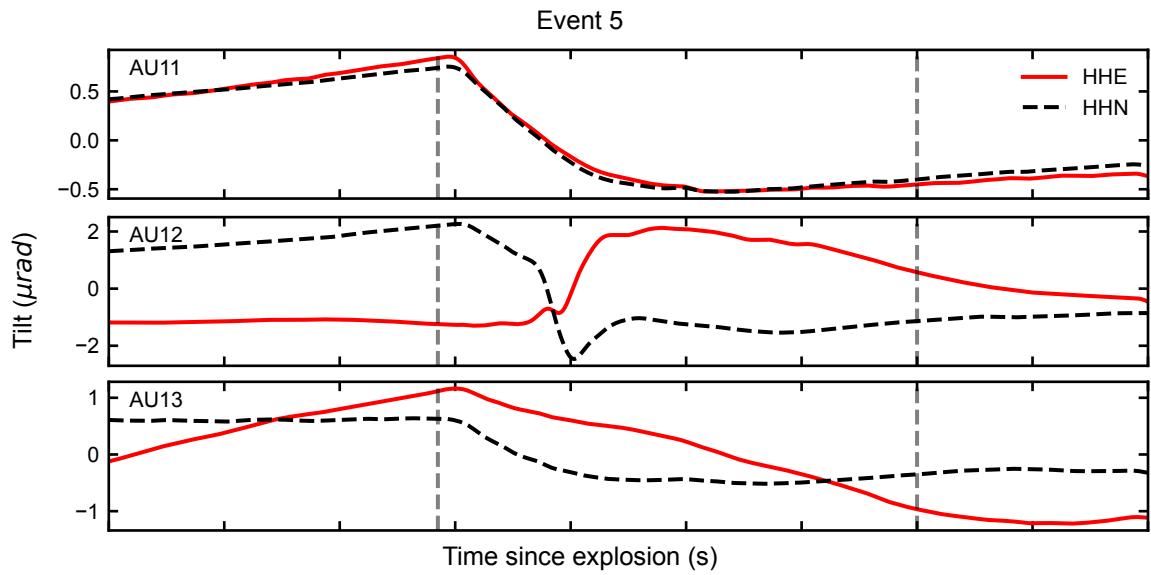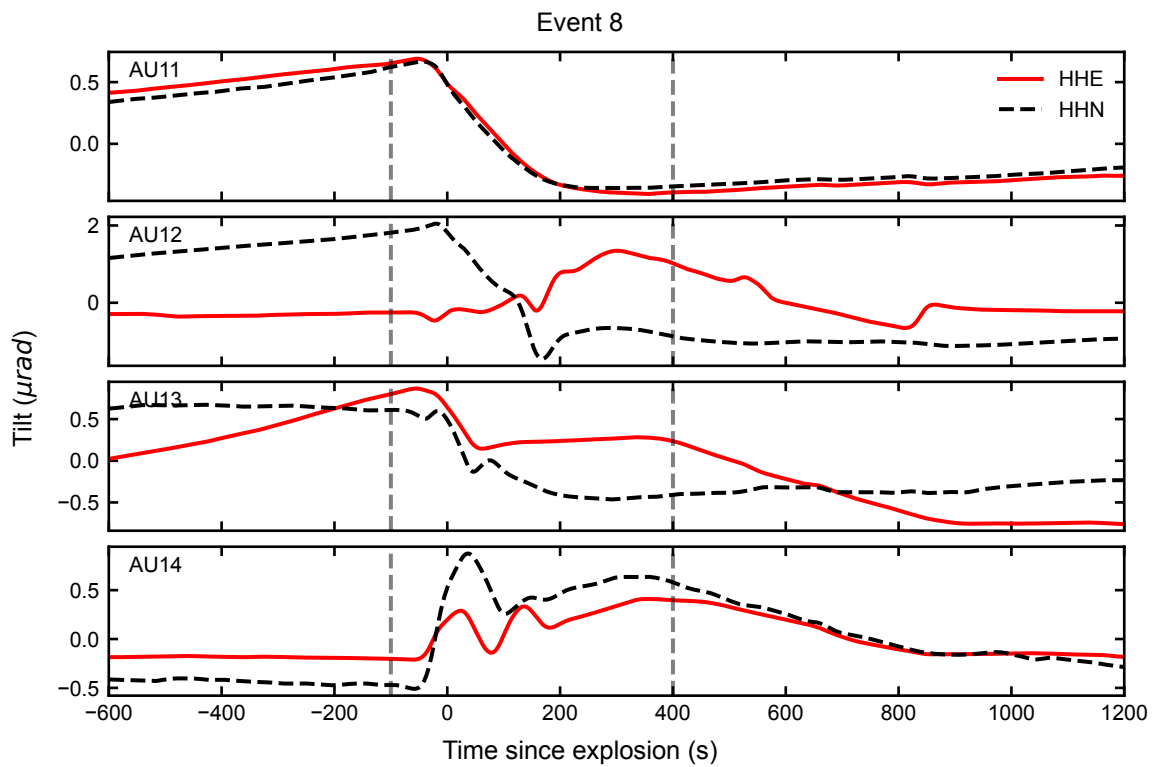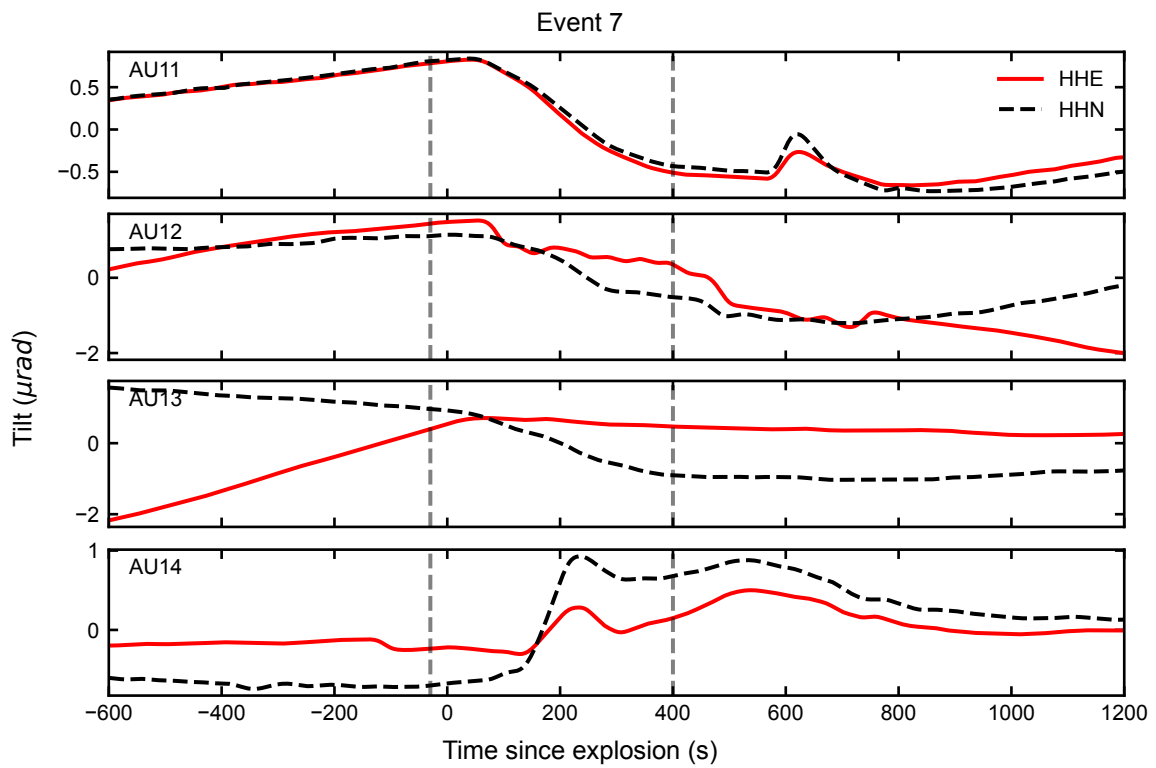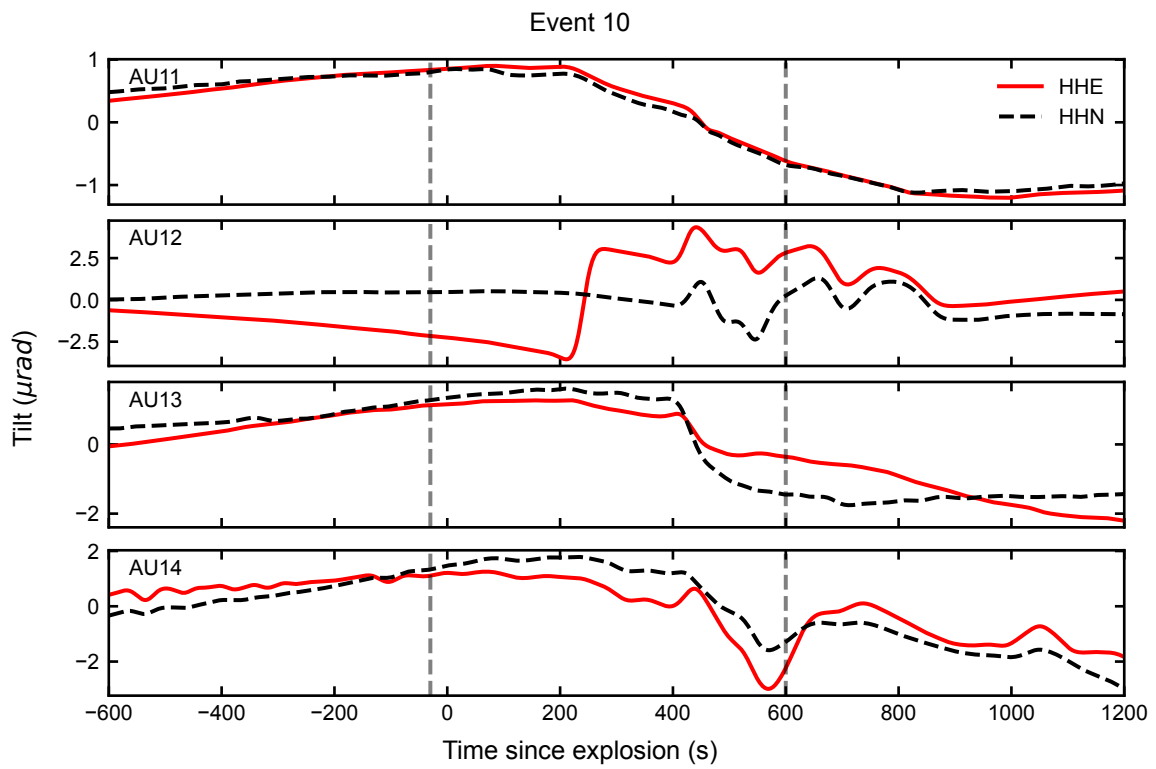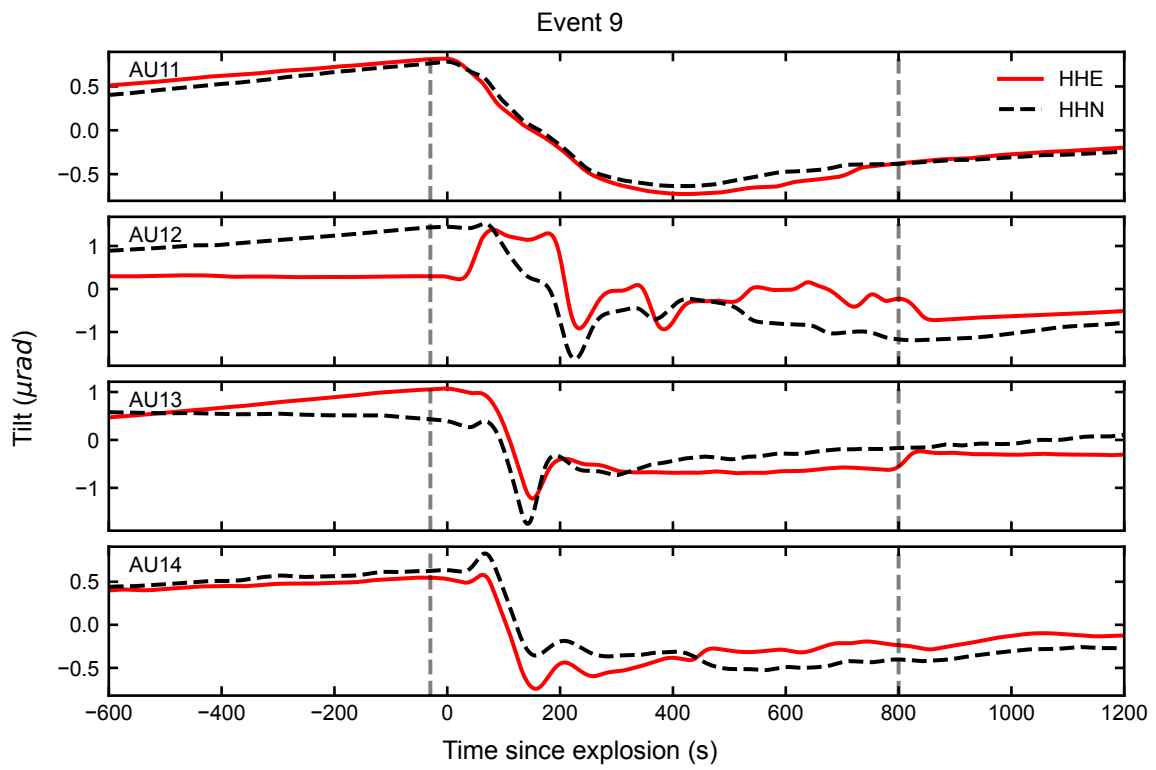
Figure A.5: Tilt time series during each explosion of the 2006 eruption of Augustine Volcano. Vertical dashed lines in each panel show the reference times between which a tilt change is calculated for each explosion.

Table A.1: UTC times of events in the catalog created by Knox *et al.* (2018) used to generate the stacked tilt time series from seismometers E1S and NKB at Mt. Erebus. (Format: yyyy-mm-dd HH:MM:SS)

2007-02-11 05:12:35
2007-02-07 02:54:19
2007-02-04 05:49:28
2007-02-16 08:34:49
2007-02-03 09:43:34
2007-02-14 05:12:42
2007-02-15 01:47:29
2007-01-25 05:04:32
2007-02-11 11:36:07
2007-02-09 11:22:08
2007-02-04 02:40:48
2007-02-22 09:05:55
2007-02-06 10:21:31
2007-02-01 12:33:34
2007-02-21 03:54:20
2007-02-14 08:09:28
2006-01-17 01:21:31
2007-01-30 08:55:51
2007-01-31 09:06:00
2007-02-10 11:32:44